Monthly Notices of the ROYAL ASTRONOMICAL SOCIETY

MNRAS **510,** 1043–1058 (2022)
Advance Access publication 2021 November 27

https://doi.org/10.1093/mnras/stab3445

The PG-RQS survey. Building the radio spectral distribution of radio-quiet quasars. I. The 45-GHz data

R. D. Baldi ,[1,2★] A. Laor,[3] E. Behar,[3] A. Horesh,[4] F. Panessa ,[5] I. McHardy[2] and A. Kimball[6]

[1]*INAF - Istituto di Radioastronomia, Via P. Gobetti 101, I-40129 Bologna, Italy*
[2]*School of Physics and Astronomy, University of Southampton, Southampton SO17 1BJ, UK*
[3]*Department of Physics, Technion, Haifa 32000, Israel*
[4]*Racah Institute of Physics, Hebrew University of Jerusalem, Jerusalem 91904, Israel*
[5]*INAF - Istituto di Astrofisica e Planetologia Spaziali, via Fosso del Cavaliere 100, I-00133 Roma, Italy*
[6]*National Radio Astronomy Observatory, 1003 Lopezville Rd, Socorro, NM 87801, USA*

Accepted 2021 November 23. Received 2021 November 23; in original form 2021 August 9

ABSTRACT

The origin of the radio emission in radio-quiet quasars (RQQs) remains unclear. Radio emission may be produced by a scaled-down version of the relativistic jets observed in radio-loud (RL) AGN, an AGN-driven wind, the accretion disc corona, AGN photon-ionization of ambient gas (free–free emission), or star formation (SF). Here, we report a pilot study, part of a radio survey ('PG-RQS') aiming at exploring the spectral distributions of the 71 Palomar–Green (PG) RQQs: high angular resolution observations (∼50 mas) at 45 GHz (7 mm) with the Karl G. Jansky Very Large Array of 15 sources. Sub-mJy radio cores are detected in 13 sources on a typical scale of ∼100 pc, which excludes significant contribution from galaxy-scale SF. For 9 sources the 45-GHz luminosity is above the lower frequency (∼1–10 GHz) spectral extrapolation, indicating the emergence of an additional flatter-spectrum compact component at high frequencies. The X-ray luminosity and black hole (BH) mass, correlate more tightly with the 45-GHz luminosity than the 5-GHz. The 45 GHz-based radio-loudness increases with decreasing Eddington ratio and increasing BH mass $M_{\rm BH}$. These results suggest that the 45-GHz emission from PG RQQs nuclei originates from the innermost region of the core, probably from the accretion disc corona. Increasing contributions to 45-GHz emission from a jet at higher $M_{\rm BH}$ and lower Eddington ratios and from a disc wind at large Eddington ratios are still consistent with our results. Future full radio spectral coverage of the sample will help us investigating the different physical mechanisms in place in RQQ cores.

Key words: galaxies: active – galaxies: jets – galaxies: nuclei – radio continuum: galaxies – X-rays: galaxies.

1 INTRODUCTION

The origin of the radio emission in radio-loud active galactic nuclei (RL AGN) is clear, luminous relativistic jets of magnetized plasma, which can extend far out, on the host galaxy scale and beyond. Conversely, radio-quiet (RQ) AGN are associated with radio emission which is typically 10^3 times weaker (as defined by Kellermann et al. 1989), in smaller structures (kpc-pc scale; e.g. Blundell et al. 1996; Nagar et al. 1999; Ulvestad et al. 2005a; Gallimore et al. 2006) with sub-relativistic velocities (e.g. Middelberg et al. 2004; Ulvestad, Antonucci & Barvainis 2005b) compared to RL AGN. The reduced sizes and low brightness of the radio emission of RQ AGN create a major challenge for detailed studies, in sharp contrast with the thoroughly studied RL AGN. The fewer radio studies of RQ AGN (e.g. Barvainis & Antonucci 1989; Kellermann et al. 1994; Barvainis, Lonsdale & Antonucci 1996; Kukula et al. 1998; Ulvestad et al. 2005a; Leipski et al. 2006; Doi et al. 2011; Padovani et al. 2011; Zakamska et al. 2016; Jarvis et al. 2019, 2021; Fawcett et al. 2020; Nyland et al. 2020; Smith et al. 2020b; Baldi et al. 2021a) generally lead to mixed results. This encourages to keep investigating it, as it indicates that the origin of the radio emission in RQ AGN is still an open question. If a number of different processes are indeed involved, then the radio band can be used to probe a range of physical processes, rather than being heavily dominated by a single process, as occurs in RL AGN (see Blandford, Meier & Readhead 2019 Panessa et al. 2019 for reviews). From large scale to small scale: (i) *host galaxy star formation* (SF) could account for the observed FIR-to-radio emission observed in active and non-active galaxies (Condon et al. 2013; Zakamska et al. 2016); (ii) an *AGN-driven wind* is expected to shock the interstellar gas, leading to particle acceleration and radio synchrotron emission, which may reach the observed flux level (Jiang et al. 2010); (iii) the intense radiation of the AGN photoionizes large volumes of ambient gas, as supported by the strength of the narrow and broad line emission observed in type-1 AGN, leading to *thermal free–free emission* in the radio band (Baskin & Laor 2021); (iv) a *scaled-down jet*, physically similar to the one in RL AGN, but much fainter, less energetic and slower (Barvainis et al. 1996; Gallimore et al. 2006; Talbot, Sijacki & Bourne 2021); (v) a tight radio/X-ray luminosity relation for AGN (∼10^{-5}; Laor & Behar 2008) similar to coronally active stars (Güdel & Benz 1993; Güdel et al. 2002) suggests that *coronal emission* from magnetic activity above the accretion disc (Field & Rogers 1993; Gallimore, Baum & O'Dea 1997) may produce the observed radio emission.

★ E-mail: ranieri.baldi@inaf.it

High resolution and high sensitivity radio observations are fundamental to determine the physical mechanism that produces the radio emission in RQ AGN. The detection of a low-brightness radio core at the centre of the radio structures, where the supermassive black hole (BH) resides, requires observations that can resolve the optically thick synchrotron source, whose size scales as $\nu^{-5/4}L^{1/2}$ (e.g. Laor & Behar 2008; Inoue & Doi 2018). Therefore, radio observations at higher-frequencies, which probe the emission on smaller scales, are required. Nevertheless, since the typical radio spectra of RQ AGN are steep in the cm-band, the detection rate could benefit from observations at intermediate radio frequencies, between the cm and mm bands. In particular, in the band, 2–0.6 cm (15–50 GHz), the probed physical scale of the radio-emitting region in nearby AGN is ∼0.01 pc, which is an order of magnitude smaller than the optically thick 5-GHz emission region.

As opposed to observations at 1.4–8.5 GHz, higher frequency observations of RQ AGN in the range 15–50 GHz are scarce. In the last decade, more efforts have been spent towards studying the radio emission from RQ AGN moving gradually from cm band to shorter wavelengths (e.g. Doi et al. 2005; Murphy et al. 2010; Park, Sohn & Yi 2013; Inoue & Doi 2014; Behar et al. 2015, 2018; Smith et al. 2016, 2020a; Ricci et al. 2019).

Radio observations at the cm-band with sub-mJy sensitivity and sub-arcsecond resolution have found extended emission on kpc scale or compact unresolved emission in the majority of RQ AGN (e.g. Nagar et al. 2002; Giroletti & Panessa 2009; Panessa & Giroletti 2013; Maini et al. 2016; Baldi et al. 2018, 2021a; Chiaraluce et al. 2019). The flat or even inverted spectrum observed at higher radio frequencies indicates a compact optically thick source (Doi et al. 2005, 2011; Behar et al. 2015, 2018), superimposed on the steep-spectrum which originates from more extended optically thin structures that dominate at lower frequencies. Such a flat-spectrum core is usually identified as the base of a possible jet or outflow, and may be located in the X-ray corona (Markoff, Nowak & Wilms 2005). To explore the nature of the radio core, the identification of such a component, resolved with high resolution observations, may help us to carry on an unbiased comparison with the well-studied cores of RL AGN. On one hand, empirical relations between the radio core luminosity and global properties of the AGN/galaxy have been found for RL AGN (e.g. radio versus BH or galaxy mass, colour, SF, Eddington ratio; see Heckman & Best 2014). On the other hand, for RQ AGN a similar study is limited because a few studies on arcsec- and mas-scale radio emission have led to conflicting or inconclusive results (e.g. the presence or not of a radio-$M_{\rm BH}$ relation; e.g. Lacy et al. 2001; McLure & Jarvis 2004; Bian et al. 2008; Panessa & Giroletti 2013; Baldi et al. 2021b). Therefore, dedicated high-resolution radio observations on large samples of RQ AGN are needed to resolve their cores, and enable us to perform an impartial comparison with RL AGN and their radio-based empirical relations.

Quasars, being luminous AGN, are perfect settings to explore the different mechanisms of radio emission. Searching for a connection between accretion/ejection properties and the radio emission in radio-quiet quasars (RQQs) is, thus, the goal of our PG-RQS (Palomar–Green Radio-Quiet SED) survey by building up the radio (from MHz to mm band) spectral energy distributions of the 71 Palomar–Green (PG) RQQs from the 87 Palomar Bright Quasar Survey at $z < 0.5$ (Schmidt & Green 1983; Boroson & Green 1992). The PG survey was the first large solid angle (10 000 square degrees) complete quasar survey, selected to be blue and point-like, and it remains the largest complete survey of optically bright quasars at $B < 16$, and therefore has no radio selection biases. It therefore provides an unbiased view of the distribution of radio emission properties of RQ AGN. The PG RQQ sample represents the most extensively studied sample of type-1 AGN and, thus, the cornerstone for quasar studies in the last decades: including, e.g. the overall SED (Neugebauer et al. 1987; Sanders et al. 1989), radio continuum and imaging (Kellermann et al. 1989, 1994; Miller, Rawlings & Saunders 1993), infrared photometry (Haas et al. 2003; Shi et al. 2014; Petric et al. 2015), optical spectroscopy (Boroson & Green 1992), optical polarization (Berriman et al. 1990), ultraviolet (UV) spectroscopy (Baskin & Laor 2005), soft X-ray spectroscopy (Brandt, Laor & Wills 2000), and radio spectral indices (Laor, Baldi & Behar 2019). From these studies, various fundamental properties were derived, such as $M_{\rm BH}$ (from broad Hβ emission line widths; Kaspi et al. 2000; Vestergaard & Peterson 2006, and from stellar velocity dispersions; Tremaine et al. 2002), accretion rates and radiative efficiencies (Davis & Laor 2011), and numerous other observed properties. This sample revealed various interesting trends, such as the eigenvector 1 (EV1) set of emission line correlations (Boroson & Green 1992), the $M_{\rm BH}$–bulge mass relation in AGN (Laor 1998), and the $M_{\rm BH}$–radio loudness relation (Laor 2000). In conclusion, for its optical selection and its large multiband coverage, the PG RQQs represent an ideal sample to search for radio-based empirical relations in the RQ regime. Although characterized by relatively high accretion rates (in Eddington units), the extreme conditions of the accretion and ejection of the PG RQQs could help in the identification of the origin of the radio emission among the different physical mechanisms. Precisely, in this work we present the results from a pilot study of 15 PG RQQs observed at 45 GHz with the Karl G. Jansky Very Large Array (VLA).

This paper is organized as follows. In Section 2, we present the project, the PG sample, and the observations. Section 3 shows the main radio properties of the sample and we seek for multiband correlations in Section 3.1. A comparison of the results with RLQs is in Section 3.2 to highlight the similarities and differences with the radio properties of RQQs, which we discuss in Section 4. We elaborate the final interpretation of the results based on the different radio production processes in RQQs in Section 4.1 and on the comparison with X-ray Binary systems (XRBs) in Section 4.2. We draw our conclusions in Section 5.

2 SAMPLE AND OBSERVATIONS

In this work, we report the A-array VLA observations for a sub-sample of 15 objects (see Table 1), randomly selected from the whole 71 RQ PG quasars at $z < 0.5$ (Boroson & Green 1992). The PG sample covers AGN over a wide range of intrinsic properties, on a wide interval of bolometric luminosities $L_{\rm Bol} \sim 10^{43}$–10^{46} erg s^{-1} and with an $M_{\rm BH}$ ranging from a few 10^6 M$_\odot$ to a few 10^9 M$_\odot$. The wealth of additional information available for this sample allows to explore possible relations between the 45 GHz emission and other emission and absorption properties, which are known to be related (e.g. Boroson & Green 1992).

Fig. 1 depicts the distributions of the main AGN luminosity estimates ([O III] emission line $L_{\rm [O\,III]}$, 4400 Å optical $L_{\rm o}$, 2–10 keV X-ray $L_{\rm X}$, bolometric luminosities[1] $L_{\rm bol}$ and BH masses $M_{\rm BH}$ taken from Boroson & Green (1992), Laor & Behar (2008) and Davis & Laor (2011) for all 71 PG RQQs. The solid histograms show the distributions of such parameters for the 15 PG RQQs studied here. We test if our pilot sample is consistent with the hypothesis that it

[1]Bolometric luminosities of the PG QSOs are calculated via broad-band (optical, UV, and X-ray) SED modelling by Davis & Laor (2011).

Table 1. VLA A-array 45-GHz properties of the observed 15 PG RQQs.

PG name (1)	Alternative name (2)	z (3)	Size pc (4)	F_{core} mJy beam^{-1} (5)	F_{tot} mJy (6)	rms mJy beam^{-1} (7)	uvtaper kλ (8)	$F_{uvtaper}$ mJy beam^{-1} (9)	$P_{45\ GHz}$ erg s^{-1} (10)
PG 0003+199	MRK 335	0.0258	52	0.50 ± 0.04	0.60	0.036	300	0.82 ± 0.08	38.52
PG 0026+129		0.1420	251	0.20 ± 0.04	0.21	0.037	300	0.53 ± 0.11	39.71
PG 0049+171	MRK1148	0.0640	124	0.63 ± 0.05	0.64	0.040	300	0.81 ± 0.10	39.46
PG 0050+124	UGC 545	0.0589	115	<0.15		0.051	500	0.30 ± 0.08	39.06
PG 0052+251		0.1544	270	0.37 ± 0.04	0.37	0.035	300	0.62 ± 0.08	40.05
PG 0157+001	MRK 1014	0.1631	282	0.48 ± 0.06	0.52	0.058	300	0.55 ± 0.11	40.22
PG 0844+349		0.0640	124	<0.06		0.020	300	<0.19	<38.46
PG 1001+054		0.1611	279	<0.06		0.019	250	0.13 ± 0.04	39.65
PG 1048+342		0.1670	288	0.17 ± 0.03	0.24	0.033	300	0.41 ± 0.12	39.80
PG 1049−005		0.3599	508	<0.11		0.035	600	0.25 ± 0.07	40.72
PG 1114+445		0.1439	254	0.13 ± 0.02	0.16	0.025	600	0.17 ± 0.05	39.54
PG 1149−110		0.0490	96	0.30 ± 0.03	0.36	0.032	600	0.31 ± 0.06	38.93
PG 1229+204	MRK 771	0.0630	122	0.27 ± 0.03	0.27	0.028	300	0.36 ± 0.08	39.12
PG 1259+593	SBS 1259+593	0.4778	602	<0.09		0.029	300	<0.24	<40.57
PG 1310−108	II SZ 010	0.0343	69	0.19 ± 0.03	0.24	0.039	300	0.38 ± 0.07	38.42

Note. Column description: (1)−(2) PG source name and alternative name; (3) redshift; (4) physical size of 100 mas; (5)–(6) 45-GHz peak flux densities (mJy beam^{-1}, derived from CASA `IMFIT` task) and total flux densities (mJy) from full-resolution maps; (7) rms (mJy beam^{-1}); (8) `UVTAPER` scale parameter; (9) 45-GHz peak flux density measured in low-resolution map (mJy beam^{-1}); (10) 45-GHz core luminosity (erg s^{-1}) from F_{core}. Upper limits are evaluated at 3σ level.

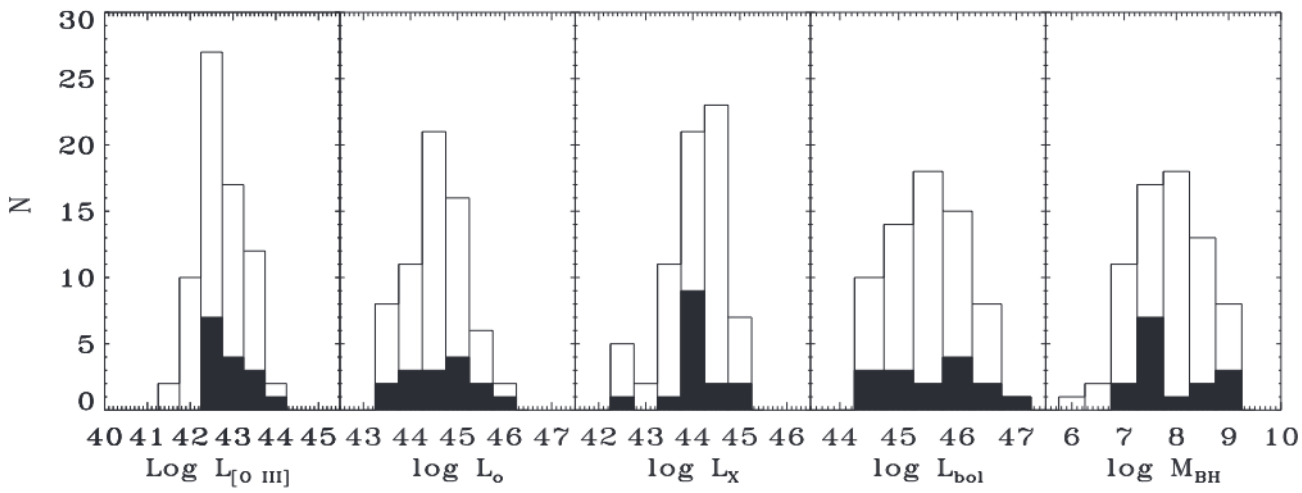

Figure 1. Distribution of the [O III] line, optical (4400 Å), X-ray (2–10 keV), bolometric luminosities (in erg s^{-1}) and BH masses (in M$_\odot$) of the whole PG RQQ sample (71 objects). The filled histograms represent the distribution of the 15 PG RQQs studied in this work. The KS tests confirm that the 15 sources are representative of the entire PG RQQ sample.

is randomly drawn from the distribution of the whole sample using the Kolmogorov–Smirnov test (KS test). The KS-test probability for each distribution is >90 per cent and confirms that 15 targets are representative of the entire PG RQQ sample.

These pilot observations of 15 PG RQQs at 45 GHz with the VLA is the first of a series of studies, part of the PG-RQS survey, aiming at exploring the PG RQQs at high and low radio frequencies with different radio arrays and angular resolutions: at arcsec resolution with *GMRT* and *LOFAR* in the MHz regime to milli-arcsec resolution with very-long baselined interferometry (VLBI) observations (such as *VLBA* and *eMERLIN*), and including high frequency observations with VLA (1–45 GHz) and with *ALMA* (85–500 GHz). An accurate determination of the broad-band SEDs of PG RQQs will allow us to probe the radial distribution of the radio emission at different scales (set by the band frequency and resolution), and constraints possible emission mechanisms.

The VLA observations of the pilot sample presented in this work were carried out in Q-band with 8-GHz bandwidth with exposure times of 12 min on source between 2016 October and 2017 January (project 16B-126). Flux and phase calibrator were observed, respectively, at the beginning of each scan (4 min) and in cycles with the target (6 min).

We used the CASA pipeline to calibrate the visibility data, including the flagging process. After obtaining the phase and amplitude solution using the calibrators, we applied them to the target source using standard procedures. Eventually, we inverted and cleaned with natural weight the visibility data to obtain the final images with an angular resolution of ∼40–80 mas and a typical rms of ∼0.02 mJy

beam^{-1} at 45 GHz. To extract the flux densities and uncertainties from the radio maps, we used IMFIT, part of the CASA VIEWER, which fits 2D Gaussians to an intensity distribution on a region selected interactively on the map. To possibly increase the chance of detecting the core and extended emission, we also reduced the map resolution by using different values of the UVTAPER parameter in the IMAGR task, ranging between 600 and 250 kλ for all the sources. This parameter specifies the width of the Gaussian function in the *uv*-plane to down-weight long-baseline data points. Smaller units of this parameter correspond to a shallower angular resolution, i.e. a larger beam size, up to a factor ∼10 larger than those reached in full resolution (i.e. ∼0.3–0.5 arcsec).

3 RESULTS

In the full-resolution maps, we detect radio emission from the central unresolved core in 10 sources with a flux density of the order of ∼0.1 mJy beam^{-1}, reaching an S/N ∼ 3–5 (see Table 1). Reducing the angular resolution by up to a factor ∼10 with UVTAPER allows us to detect three additional objects, PG 0050+124,PG 1001+054, and PG 1049−005. However, two objects, PG 0844+349 and PG 1259+593, remain undetected. In conclusion, we detect a 45-GHz radio core in 13 out of 15 sources (86 ± 7 per cent of our sample).

Fig. 2 presents the full-resolution radio images at 45 GHz of our sample. For the sources not detected in full resolution, we display the *uv*-tapered images. Most of the targets appear unresolved or slightly resolved at the full resolution on 50–100 mas (Table 2) which corresponds to a few hundred pc (Table 1). The ratio between total and peak flux densities for these sources is close to unity, suggesting their structure is unresolved. Four sources (PG 0049+171, PG 0050+124, PG 0157+001, and PG 1114+445) show a marginal elongation of the radio core emission. The *uv*-tapered maps do not show any significant evidence of extended emission in any of the targets of the sample.

With the final goal of deriving the radio cm-wavelengths SEDs, we search in the literature and VLA image archive[2] for radio data below 45 GHz, both at the highest resolution with A array, and at the lower resolution with B-C-D arrays (see Table 3, and references therein). Fig. 3 displays the radio SEDs of the 15 objects in the frequency range 1.4–45 GHz. Filled points mark the highest resolution A array data, and the crosses represent the measurements at lower resolutions. There is a rich variety of spectral shapes ($F_\nu \sim \nu^\alpha$) across the 1–45 GHz band (Table 4). We define the broad-band spectral class of the sources, based on both the A-array and the lower resolution VLA data available for the targets:

(i) *steep (S)*: if the radio SED is characterized by a steep spectral index ($\alpha < -0.5$) in both high and low resolution data: PG 0003+199, PG 0050+124, PG 0157+001, PG 1149−110. We also include PG 0844+349 into this category because with only one detection (at low resolution at 5 GHz) the estimated spectral slope can be considered as upper limit.

(ii) *flat or slightly inverted (F)*: if the radio SED is characterized by a flat spectral index ($0.1 > \alpha > -0.5$) in both high and low resolution data (or only in high resolution if the low resolution data do not provide detections): PG 0049+171, PG 1048+342, PG 1049−005, and PG 1310−108.

(iii) *a broken power-law (S + F)*: the combination of steeper lower frequency spectrum and a flatter higher frequency spectrum at either low or high resolution data: PG 0026+129, PG 0052+251, PG 1001+054, PG 1114+445, and PG 1229+204.

We abstain from the spectral classification of PG 1259+593 because of the lack of detections from the available radio data. Note that these radio SEDs do not account for radio core variability, which is known to be present by as much as a factor of 2–3 (Falcke et al. 2001; Barvainis et al. 2005; Mundell et al. 2009; Baldi et al. 2015; Behar et al. 2020; Nyland et al. 2020), nor the different angular resolutions ranging from 1.3 to 0.40 arcsec with A-array observations in different bands.

The radio SEDs presented in Fig. 3 suggest that the typical radio spectrum of PG RQQs consists of a combination of at least two components,[3] a steep-spectrum component which dominates at low frequencies and low resolution, and a flat-spectrum component (typically unresolved) which emerges at high resolution and at high frequencies (Table 4). At least for 9 sources, a flat-spectrum radio component emerges at high radio frequencies. Is this because one component is brighter, or because the other component is weaker, relative to the emission in other bands?

Fig. 4 shows the 5–45 GHz spectra of the detected PG RQQs normalized by the flux densities in the optical band from Kellermann et al. (1989) at 4400 Å (a proxy of radio loudness). The plot shows that, the spectral steepness of the RQQs is due to the brighter 5-GHz core component, rather than a dimmer 45-GHz component. In turn, the flattening of the RQQ spectra is the result of the weakening of the steep-spectrum component. These results would suggest that steep-spectrum objects have an additional mechanism which produces optically thin emission, which adds to the flat-spectrum optically thick emission that most of objects have.

3.1 Multiband correlations

As higher energy photons are expected to originate from inner regions of the nucleus (accretion disc, jet base, etc.), early studies revealed that radio properties in RQQs are linked to the accretion/ejection activity, derived from high-energy bands (e.g. optical, X-ray; Boroson & Green 1992; Laor & Behar 2008). In addition, it has been recently found the radio spectral slopes of RQQs can also depend on several AGN parameters, which in turn are linearly combined in the EV1 diagram (see Laor et al. 2019, and references therein).

To derive possible meaningful correlations between the 45-GHz emission with that in other lower frequency VLA bands, we calculate the Q-band luminosities, νL_ν ($\equiv P_{45\,\mathrm{GHz}}$) in units of erg s^{-1}, which covers the range $\sim 38.4 < \log L_{45\,\mathrm{GHz}} < 40.7$. We also use the core luminosity densities at 5 GHz, νL_ν ($\equiv P_{5\,\mathrm{GHz}}$ from Kellermann et al. 1989) which covers the range $\sim 37.6 < \log P_{5\,\mathrm{GHz}} < 40.1$. Note that although we always use the A-configuration for both the Q band and the C band observations for the following radio luminosity plots (unless explicitly expressed), the Q band resolution is 40–80 mas versus ∼0.3 arcsec in the C band, due to the factor 9 drop in frequency. Thus, if the radio emission is extended, the derived slope between the two bands will be steeper than the intrinsic core slope. In this scenario, since extended radio emission is almost always characterized by an optically thin steep power law, this possible bias will not change the character of the 45-GHz emission. This aperture bias does not work in the opposite direction, and an observed flat-spectrum is inevitably flat (or even flatter if it is contaminated by a

[2] https://archive.nrao.edu/archive/archiveimage.html

[3] The spectral slopes are obtained by fitting the censored radio data in Fig. 3. In case of the presence of non-detections, the spectral slope is rough estimates, measured by assuming upper limits as detections for simplicity.

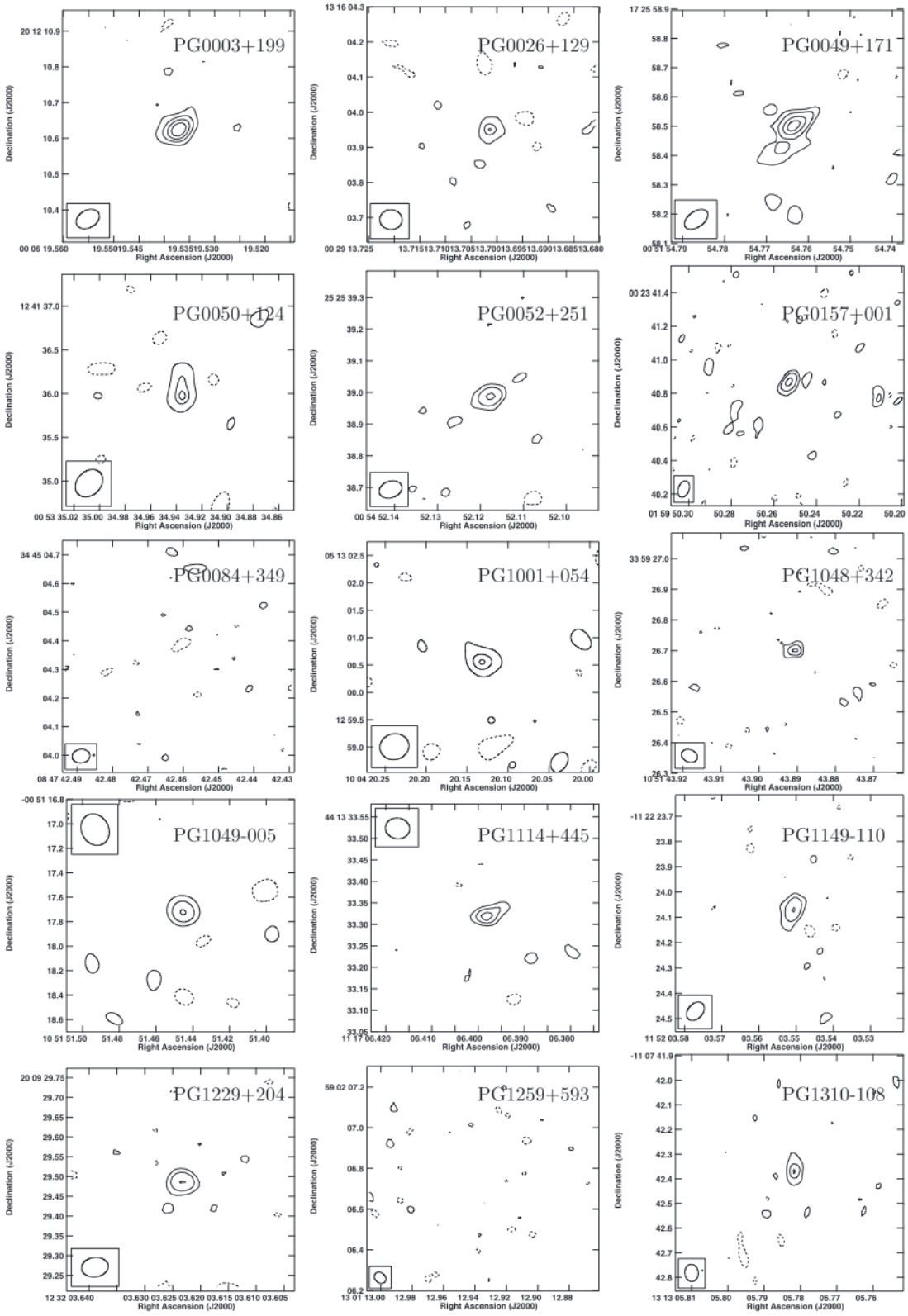

Figure 2. The A-array VLA 45-GHz maps of the 15 PG RQQs in full resolution (40–80 mas), except for PG 0050+124, PG 1001+054, PG 1049−005 for which we present the *uv*-tapered map where the core emission is detected at a lower resolution (<0.5 arcsec). Two objects, PG 0844+349 and PG 1259+593, are not detected. The map properties (beam and contour levels) are presented in Table 2.

Table 2. Parameters of the JVLA 45-GHz maps (Fig. 2).

PG name	Beam	PA	Contour levels
PG 0003+199	0.069 × 0.049	− 60.6	0.09.5 × (−1,1,2,3,4)
PG 0026+129	0.064 × 0.056	87.3	0.080 × (−1,1,2,2.4)
PG 0049+171	0.090 × 0.053	− 54.3	0.085 × (−1,1,2,4,6)
PG 0050+124	0.35 × 0.27	− 44.5	0.25 × (−1,1,2,2.5)
PG 0052+251	0.074 × 0.052	− 71.5	0.080 × (−1,1,2,4)
PG 0157+001	0.10 × 0.073	− 28.5	0.10 × (−1,1,2,4)
PG 0844+349	0.062 × 0.048	− 83.4	0.047 × (−1,1)
PG 1001+054	0.53 × 0.47	− 75.6	0.050 × (−1,1,2,2.5)
PG 1048+342	0.054 × 0.040	67.2	0.077 × (−1,1,1.5,2)
PG 1049−005	0.27 × 0.22	28.2	0.12 × (−1,1,1.5,2)
PG 1114+445	0.057 × 0.048	82.2	0.055 × (−1,1,1.5,2)
PG 1149−110	0.083 × 0.058	− 41.2	0.075 × (−1,1,2,4)
PG 1229+204	0.068 × 0.049	− 82.7	0.065 × (−1,1,2,4)
PG 1259+593	0.061 × 0.050	48.5	0.070 × (−1,1)
PG 1310−108	0.070 × 0.054	5.3	0.065 × (−1,1,2,2.8)

Note. Column description: (1) source name; (2) FWHM of the elliptical Gaussian restoring beam (in arcsec) of the maps presented in Fig. 2; (3) PA of the restoring beam (degree); (4) radio contour levels (mJy beam^{-1}).

steep component) and must therefore originate from an optically thick compact source. An intrinsic compact source will remain unresolved in both bands, and the measured slope will be unaffected by the different resolutions.

Fig. 5 depicts the correlations of $P_{5\,\mathrm{GHz}}$ (left-hand panel) and $P_{45\,\mathrm{GHz}}$ (right-hand panel) with the typical calorimeters of AGN strength: the X-ray (2–10 keV) luminosity L_X, the optical luminosity L_o, the bolometric luminosity L_{bol} and the [O III] line luminosities $L_{[\mathrm{O\,III}]}$. Since several upper limits are present in the data sets, the statistical significance of each correlation is measured by using a censored statistical analysis (ASURV[4]; Lavalley, Isobe & Feigelson 1992) which takes into account the presence of upper limits. We used the `schmittbin` task (Schmitt 1985) to calculate the associated linear regression coefficients for two sets of variables. Effectively, we carried out this procedure twice, obtaining two linear regressions: first, we consider the former quantity as the independent variable and the latter as the dependent one and second switching the roles of the variables. The best fit is represented by the bisector of these two regression lines. This followed the suggestion of Isobe et al. (1990) that considers such a method preferable for problems that require a symmetrical treatment of the two variables. To estimate the quality of the linear regression, we used the generalized Kendall's τ test (Kendall 1983) (task `bhkmethod`) valid for sample smaller than 30 targets as in our case and the associated probability that the correlation is fortuitous. We have also measured the (maximum) rms of the correlations, by assuming that censored data are detections. Table 5 provides the statistical parameters, slope, and intercepts of the linear regressions we evaluate in this work.

Fig. 5 shows that $P_{45\,\mathrm{GHz}}$ presents tighter correlations with L_X, L_{opt}, L_{bol}, and $L_{[\mathrm{O\,III}]}$ compared to those with $P_{5\,\mathrm{GHz}}$. A clear outlier from the X-ray–radio regressions is PG 1001+054, which is known to be significantly X-ray absorbed (Schartel et al. 2005). Therefore, we excluded this target in the statistical analysis. From all correlations presented in Fig. 5, the tightest fit is $P_{45\,\mathrm{GHz}}$-L_X (rms $= 0.117$) and the most statistically significant one is $P_{45\,\mathrm{GHz}}$– $L_{[\mathrm{O\,III}]}$ (P $= 0.0003$). The strength of these two relations is remarkable, given the fact that the X-ray and optical nuclei are generally more variable (variability amplitudes, typically, of a factor of several, up to ∼50; e.g. Guainazzi, Jimenez-Bailon & Piconcelli 2006; Markowitz & Edelson 2004; Paolillo et al. 2004; Saez et al. 2012; Lanzuisi et al. 2014) than those detected in the radio-band (variability amplitudes of a factor of few; e.g. Barvainis et al. 2005; Mundell et al. 2009).

3.2 Comparison with PG radio-loud quasars

The PG quasar sample (Boroson & Green 1992) also includes 16 RL AGN. Below we compare their 45 GHz properties with those of the PG RQQs to search for significant similarities and differences between the two quasar samples. This aims at investigating the nature of the radio emission in RQQs in relation to the well-studied relativistic collimated jet emission of RL AGN.

We obtain 45-GHz VLA observations in A and B configuration for 8 RLQs from the literature (see Table 6). For the remaining 8 sources, the 45 GHz flux densities are roughly estimated by a power-law extrapolation of their radio spectra (taken from the NASA/IPAC Extragalactic Database[5]) from lower frequencies.[6] The typical spectral coverage is from 74 MHz to 8.5 GHz and in some cases up to the 31.4 GHz. The typical error bars on the 45-GHz flux densities for those sources are estimated as a factor 2 of the measurements (∼0.3 in logarithmic scale).

Fig. 6 compares $L_{45\,\mathrm{GHz}}$ versus $L_{5\,\mathrm{GHz}}$ (erg s^{-1} Hz^{-1}) of the PG RLQs and RQQs. The RLQs are typically ∼1000 times brighter than the RQQs at both 5 GHz and at 45 GHz. The scatter of the relation between log $L_{45\,\mathrm{GHz}}$ and log $L_{5\,\mathrm{GHz}}$ of the PG RQQs ($\sigma = 0.29$) is smaller than that for that RLQs ($\sigma = 0.41$). This may result from enhanced core variability and orientation-dependent Doppler beaming or from the spectral extrapolation scatter, valid for RLQs.

Since the BH mass has been found to be a crucial quantity for modelling and interpreting observations in the framework of jet launching mechanism of RL AGN (Blandford & Znajek 1977; Cattaneo & Best 2009), here we compare the radio luminosities of the PG quasars with M_{BH}. Fig. 7 shows the dependence of $P_{45\,\mathrm{GHz}}$ and $P_{5\mathrm{GHz}}$ on M_{BH} for the RL and RQ PG quasars. The RQQs show strikingly tight linear correlations, (P $= 0.0023$ for $P_{45\,\mathrm{GHz}}$) with a smaller scatter at 45 GHz than at 5 GHz, in the form $P_{45\,\mathrm{GHz}} \propto M_{BH}^{1.17}$, which is consistent within the errors with the slope of the M_{BH}-radio correlation established for nearby RQ AGN observed with eMERLIN (Baldi et al. 2021b). For RLQs, the radio-BH relations have significantly larger scatter and are not statistically significant, with P values of only $\gtrsim$0.07. Apart from possible large systematic errors due to the SED-extrapolated 45-GHz emission, the most plausible physical reason of a larger scatter for the RLQ relation than that of RQQs is the higher variability amplitude of RLQs due to Doppler boosting.

To derive the spectral slopes between the C and Q bands ($F_\nu \sim \nu^\alpha$), we used the uv-tapered Q-band core flux densities which are extracted from the images with a resolution comparable with the

[4]ASURV package has been used within the PyRAF software (Science Software Branch at STScI 2012).

[5]NED, http://ned.ipac.caltech.edu

[6]This method is supported by the fact that all the RLQs are Fanaroff–Riley type-II radio galaxies, which have powerful extended steep-spectrum jets which dominate the entire broad-band radio SED. As a counter-check, the 45-GHz VLA luminosities of the 8 RLQs taken from literature are consistent with the values extrapolated from the data from NED within the scatter of the power-law relation.

Table 3. VLA peak flux densities in mJy of the 15 observed PG RQQs from 1.4 to 15 GHz taken from VLA archive and literature.

	Array-A VLA flux densities			B-C-D VLA flux densities			
Frequency:	1.4GHz	5 GHz	8.5 GHz	1.4GHz	5 GHz	8.5 GHz	15 GHz
Resolution:	1″.3	0″.33	0″.20				
Object	F_ν	F_ν	F_ν	F_ν	F_ν	F_ν	F_ν
PG 0003+199	6.74 ± 0.11^a	3.03 ± 0.10^b	2.05 ± 0.1^c	7.3 ± 0.5^f	3.92 ± 0.1^b	2.23 ± 0.25^g	
		3.49 ± 0.05^e			3.58 ± 0.1^e		
PG 0026+129	2.4 ± 0.7^d	0.20 ± 0.06^b	0.17 ± 0.05^e	7.1 ± 0.5^f	5.10 ± 0.1^b	2.37 ± 0.06^e	
PG 0049+171	0.44 ± 0.12^a	0.66 ± 0.10^b		$<2.5^f$	0.64 ± 0.10^b	0.66 ± 0.10^g	
PG 0050+124	5.1 ± 0.4^d	1.80 ± 0.10^b	0.9 ± 0.2^d	6.22 ± 0.35^h	2.60 ± 0.11^b		1.06 ± 0.32^h
		2.4 ± 0.3^d					
PG 0052+251	1.1 ± 0.4^d	0.42 ± 0.10^b	0.7 ± 0.1^d	1.59 ± 0.14^a	0.74 ± 0.10^b		
		0.58 ± 0.03^e			0.61 ± 0.03^e		
PG 0157+001		5.58 ± 0.06^b	2.98 ± 0.03^e	22.5 ± 0.8^h	7.88 ± 0.26^h	4.23 ± 0.03^e	2.04 ± 0.32^h
PG 0844+349		$<0.25^b$		$<0.38^i$	0.31 ± 0.06^b		
PG 1001+054		$<0.25^b$		$<2.5^f$	0.80 ± 0.1^b	0.64 ± 0.3^a	
PG 1048+342				$<0.42^i$	$<0.19^b$	$<0.12^a$	
PG 1049−005		0.22 ± 0.03^e		0.82 ± 14^i	0.48 ± 0.03^b	0.37 ± 0.07^a	
PG 1114+445		0.20 ± 0.06^b		0.71 ± 0.12^i	0.22 ± 0.06^b		
PG 1149−110	3.1 ± 0.8^d	1.20 ± 0.20^d	1.3 ± 0.1^d	9.7 ± 0.6^f	2.60 ± 0.1^b	0.54 ± 0.02^a	
		1.08 ± 0.06^e	0.99 ± 0.04^a		1.94 ± 0.1^e		
		1.0 ± 0.1^b					
PG 1229+204		0.30 ± 0.06^b		2.8 ± 0.4^f	0.67 ± 0.1^b		
PG 1259+593		$<0.25^b$		$<0.45^i$	$<0.3^a$		
PG 1310−108		$<0.25^b$		$<2.5^f$	0.26 ± 0.06^b	$<0.15^a$	

Notes. Upper limits are evaluated at 3σ level. References: [a]map obtained from the image VLA archive, [b]Kellermann et al. (1989), [c]Kukula et al. (1995); [d]Kukula et al. (1998); [e]Leipski et al. (2006); [f]Condon et al. (1998); [g]Barvainis et al. (2005); [h]Barvainis & Antonucci (1989); [i]Becker, White & Helfand (1995).

C band data, ∼0.3–0.5 arcsec. The $\alpha_{5-45\mathrm{GHz}}$ values range between −1 and 0.3 (Table 4, with typical errors of 30 per cent), a narrower interval than the spectral indices derived at lower radio frequencies, 5–8.5 GHz (Laor et al. 2019). We compared the 5–45 GHz indices with the parameters of the EV1 set of correlations (Boroson & Green 1992), i.e. Hβ full width at half-maximum (FWHM), Eddington ratio L/L_{Edd}, and M_{BH}, in analogy to the analysis done by Laor et al. (2019) (Fig. 8, left-hand panels). We fit the censored data, and the derived relations between the radio slopes and the three quantities for the RQQs appear to be statistically weak (with probabilities of fortuitous correlations higher than 0.02; see Table 5). General trends have been found: the radio slope generally seems to flatten for larger Hβ width, smaller L/L_{Edd} and higher M_{BH}, similarly to what was seen by Laor et al. (2019), but with lower statistical significance. For a comparison with RLQs, we analogously fit their censored $\alpha_{5-45\mathrm{GHz}}$ and EV1 quantities (Fig. 8, right-hand panels). The statistics of the regressions are even lower than those of RQQs, but we can conclude that RLQs generally display opposite trends to the ones obtained with RQQs, which could slightly strengthen the different radio physical properties of RQQs and RLQs. The statistically strongest relation (P ∼ 0.02) is $\alpha_{5-45\mathrm{GHz}}$ − Hβ FWHM, where RQQs and RLQs clearly reveal opposite regressions.

As the radio loudness has been related to the accretion properties and BH mass in the past (e.g. Nelson 2000; Best et al. 2005; Ho 2008; Heckman & Best 2014; Chang et al. 2021), we also investigate the 45 GHz-based radio loudness of the PG quasars, measured as $P_{45\,\mathrm{GHz}}/L_{\mathrm{o}}$ and $P_{45\,\mathrm{GHz}}/L_{\mathrm{X}}$, respectively, as function of L/L_{Edd} and M_{BH} (Fig. 9). We find a tight $P_{45\,\mathrm{GHz}}/L_{\mathrm{o}} - L/L_{\mathrm{Edd}}$ correlation (left-hand panel, P = 0.0093, rms = 0.245), where the RQQs become quieter with increasing L/L_{Edd}. At $L/L_{\mathrm{Edd}} \gtrsim 0.3$, which is roughly the value when the spectral indices steepen, $\lesssim$0 (Fig. 8), we get that $P_{45\,\mathrm{GHz}}/L_{\mathrm{o}} < 10^{-5}$, the typical value expected for the corona disc emission. In addition, we also find that $P_{45\,\mathrm{GHz}}/L_{\mathrm{X}}$ is linearly correlated with M_{BH} (P = 0.0078, rms = 0.322): RQQs become louder with increasing M_{BH}. Since 45-GHz luminosities have been found to correlate with the optical and X-ray luminosities (despite not with a slope of unity), the dependence of these luminosity ratios with L/L_{Edd} and BH mass highlights a second-order effect in the radio emission production in RQQs. A larger sample of RQQs would still be necessary to confirm this result. Conversely, RLQs do not show statistically significant correlations. However, we can note that at $M_{\mathrm{BH}} > 10^9$ M$_\odot$ all PG quasars become RL, and their $P_{45\,\mathrm{GHz}}/L_{\mathrm{X}}$ jumps by a factor of ∼30, compared to the RQQs of our sample.[7]

4 DISCUSSION

The overall 1.4–45 GHz spectra of the 15 PG RQQs studied here indicate that two main components shape the SEDs of most of the sources: a steep-spectrum and a flat-spectrum component which dominates, respectively, at low and high radio frequencies. The 45-GHz emission is generally dominated by the latter, which in some objects extends down to 5 GHz (at least in 9 sources), in particular in high resolution observations. A flat-spectrum core suggests an optically thick source, which implies a physically compact source with a size ∼0.001–0.02 pc (e.g. equation 22 in Laor & Behar 2008).

A compact source which characterizes the 45-GHz emission, is also supported by two further results from this study. In fact, most of our sources are unresolved, i.e. should be smaller than ∼50 mas, which corresponds to physical sizes smaller than ∼50–100 pc. Only in two objects (PG 0844+349 and PG 1259+593) an unresolved core is not detected. These two sources also lack of further detections at

[7]The standard 5 GHz-to-optical radio-loudness parameter drops by a factor of ∼1000 from RLQs and RQQs at $M_{\mathrm{BH}} \sim 10^9$ M$_\odot$.

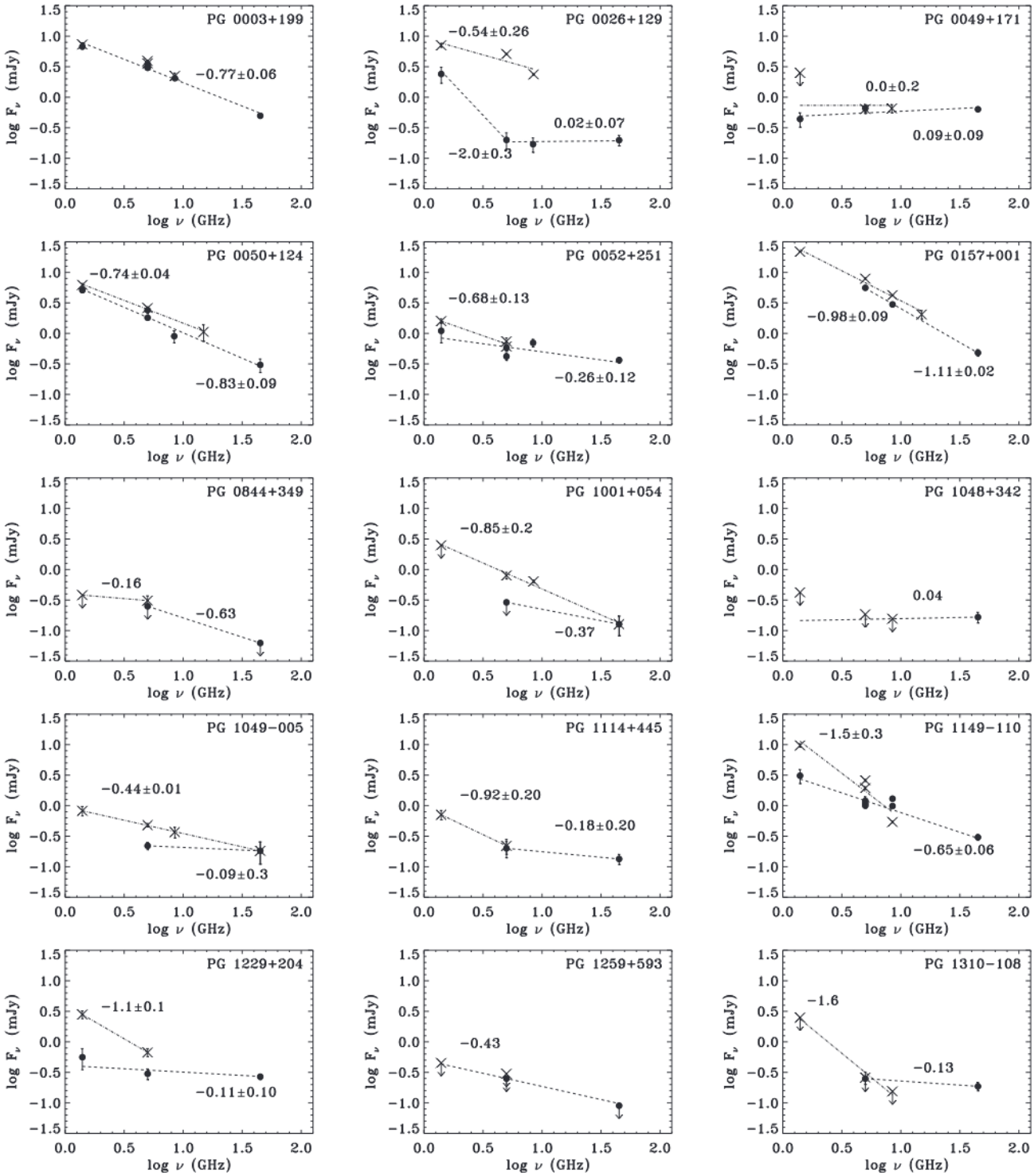

Figure 3. A compilation of the overall 1.4–45 GHz SED of the 15 PG RQQs presented in this work based on VLA data. Filled points mark the highest resolution, A array, data, and the crosses measurements at lower resolutions (B-C-D arrays). The dot–dashed line shows the spectral slope for the VLA low-resolution data, while the dashed line represents the spectral properties of the unresolved core component at VLA high resolution. The corresponding values reported on the plot are the spectral indices derived by fitting the censored data.

high resolution and at lower radio frequencies, thus giving a coarse charaterization of their radio spectra.

The other indirect evidence for the general compact nature of the 45 GHz emission comes from the tight correlation of $P_{45\,\mathrm{GHz}}$ with the direct AGN luminosities L_X, L_o, L_{bol}, and $L_{[O\,III]}$, in particular when compared with the somewhat-weaker correlations of $P_{5\mathrm{GHz}}$ with these quantities. This result is notable given the ∼20–30 yr time span between the 45 GHz and the earlier optical and X-ray observations, and is similar to previous studies that have found striking radio–X-ray correlations at even smaller radio scales and at lower luminosities (e.g. Panessa & Giroletti 2013; Panessa et al. 2015). As it occurs at longer cm-band wavelengths, the 5 GHz luminosity may depend

Table 4. Radio spectral indices of the PG 15 RQQs.

Name	1 comp	2 comp	S/F	$\alpha_{5-45\mathrm{GHz}}$
PG 0003+199	-0.77 ± 0.06		S	-0.83
PG 0026+129	-0.54 ± 0.26	0.02 ± 0.07	$S+F$	0.20
PG 0049+171	0.0 ± 0.2	0.09 ± 0.09	F	0.25
PG 0050+124	-0.74 ± 0.04	-0.82 ± 0.09	S	-0.90
PG 0052+251	-0.68 ± 0.13	-0.26 ± 0.12	$S+F$	-0.26
PG 0157+001	-0.98 ± 0.09	-1.11 ± 0.02	S	-0.91
PG 0844+349	-0.16	-0.63	S	<-0.32
PG 1001+054	-0.85 ± 0.20	-0.37	$S+F$	-0.71
PG 1048+342	0.04		F	>0.25
PG 1049−005	-0.44 ± 0.01	-0.09 ± 0.30	F	-0.04
PG 1114+445	-0.92 ± 0.20	-0.18 ± 0.20	$S+F$	-0.06
PG 1149−110	-1.5 ± 0.3	-0.65 ± 0.06	S	-0.86
PG 1229+204	-1.1 ± 0.1	-0.11 ± 0.10	$S+F$	-0.14
PG 1259+593	-0.43		?	
PG 1310−108	-1.6	-0.13	F	-0.17

Note. Column description: (1) PG source name; (2)–(3) spectral slopes of the first and second radio components, estimated, respectively, typically at lower frequencies ($\lesssim$5 GHz) and lower resolution (VLA B-C-D array), and higher radio frequencies ($\gtrsim$5 GHz) and higher resolution (VLA A array) (see Fig. 3); (4) general radio SED dominance: S for steep-spectrum component, F for flat-spectrum component; $S+F$ combination of a steep- and flat-spectrum component; (5) spectral indices between 5 and 45 GHz, with typical errors of 30 per cent.

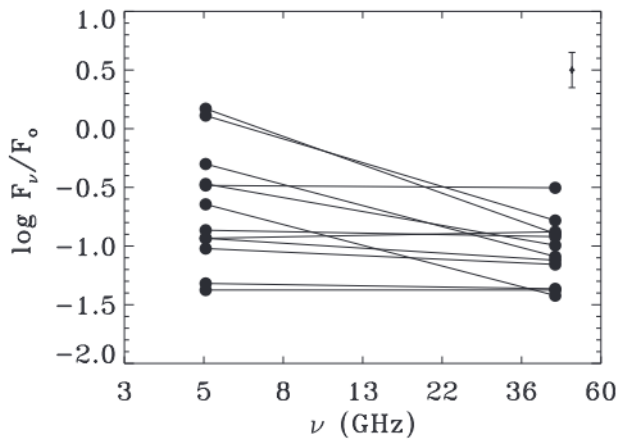

Figure 4. Radio flux densities at 5 and 45 GHz (in logarithmic scale) normalized by the optical 4400Å flux density (i.e. ratio between the radio and optical flux densities) for the RQQs which are detected in Q-band. At the top-right corner, we draw the typical error bar on the y-axis, ∼0.2–0.3. The plot shows that RQQs tend to have steeper radio spectra because of brighter 5 GHz emission relative to the optical, rather than dimmer 45 GHz emission.

more on the host galaxy properties, if it is produced e.g. by an AGN-driven wind that shocks the host interstellar medium (ISM), or nuclear SF (e.g. Zakamska et al. 2016; Mancuso et al. 2017; Richards et al. 2021). Instead, at higher radio frequencies, at 45 GHz in our case, the radio emission may originate from an inner physical region at the accretion disc scale, e.g. from coronal disc emission, or a weak jet (e.g. Chiaraluce et al. 2020; Smith et al. 2020b; see Section 4.1 for the discussion on the radio origin), and is set by the AGN properties.

The genuine compact nature of the 45 GHz emission of the PG RQQs which clearly show spectral flattening at high frequencies, could be tested using VLBI observations. A few available VLBI studies of RQ AGN (e.g. Blundell & Beasley 1998; Ulvestad et al. 2005b; Doi et al. 2013) reveal a mas-scale (∼*pc*) flat-spectrum compact source, which extrapolates well to the observed higher radio-frequency emission (Laor et al. 2019). Future VLBI observations of the PG RQQs, part of our survey, will confirm their compactness.

Although not statistically very robust, the suggested relations between $\alpha_{5\text{-}45}$ and the Hβ FWHM, L/L_{Edd} and M_{BH} are consistent with the results found by Laor et al. (2019) for the PG quasars by using radio slopes at 5–8.5 GHz. The most significant relation is the steepening of the radio slopes of RQQs with $L/L_{\mathrm{Edd}} > 0.3$ and low Hβ widths. This Eddington ratio limit can be interpreted at the condition of a radiatively efficient accretion disc, required to launch a radiation pressure driven wind, which then shocks the host ISM and produces a steep-spectrum extended synchrotron source (King et al. 2013; Zakamska & Greene 2014; Nims, Quataert & Faucher-Giguère 2015). Conversely, the dependence on Hβ FWHM is not simply interpretable as an orientation effect, as flatter spectra would be expected in a polar view. The weaker correlations found here than the ones found with $\alpha_{5\text{-}8.5}$ (Laor et al. 2019) may result from the fact that $\alpha_{5\text{-}45}$ is more an estimate of the relative contributions of the steep and flat sources. In contrast, the radio slope at 5–8.5 GHz, is a more physical estimate of the nuclear properties and likely a more accurate measure of the outflow characteristics.

A remarkable result of this study is the presence of unprecedentedly tight correlation between the 45-GHz radio luminosity and the BH mass for our sample, with a dependence similar to what has been found for local low-luminosity RQ AGN, but with a larger scatter (Baldi et al. 2021b). The connection between the mas-scale radio properties (luminosity, spectral slope, radio loudness) and the BH mass for our sample suggests that the latter should play an important role at setting the mechanism of radio production in RQQs (in jet and wind scenarios). In addition, the radio loudness parameter has been found to increase with BH mass and decrease with the Eddington ratio, consistent with previous studies (e.g. Ho 2002; Merloni, Heinz & di Matteo 2003; Nagar, Falcke & Wilson 2005; Sikora, Stawarz & Lasota 2007; Gürkan et al. 2019; Chiaraluce et al. 2020). However, in support of a distinct origin of the radio emission between RLQs and RQQs is the different (even opposite) trends with radio slopes and BH mass. Therefore, even in the same quasar regime (at high Eddington ratios), the radio outflow of RQQs must differ in terms of its driving mechanism compared to the strong jet observed in RLQs.

Based on the statistical significance of the tested correlations, the 45-GHz emission in PG RQQs is mainly driven by the X-ray radiation and the BH mass. The X-ray emitting corona coincide with the jet base for RLQs (Markoff et al. 2005) and with the physical region where 45-GHz emission is produced, more internal than the 5-GHz core, for RQQs (Laor & Behar 2008). The similarity of the 45-GHz emitting region of RLQs and RQQs would possibly suggest that the corona is playing an important role in the radio emission production in quasars and the properties of such a corona could account for the transition from a relativistic jet in case of RLQs to a sub-relativistic outflow in case of RQQs at high radio frequencies.

4.1 Origin of the 45-GHz emission in RQQs

Here, we explore the various possible scenarios of radio-emitting physical mechanisms (see Panessa et al. 2019), which may account for the results we find in this work.

(i) *Star formation*. A compact nuclear starburst could be scarcely consistent with the flat-spectrum unresolved cores we find. High SF rate is generally expected at high accretion-rate AGN, as expected in

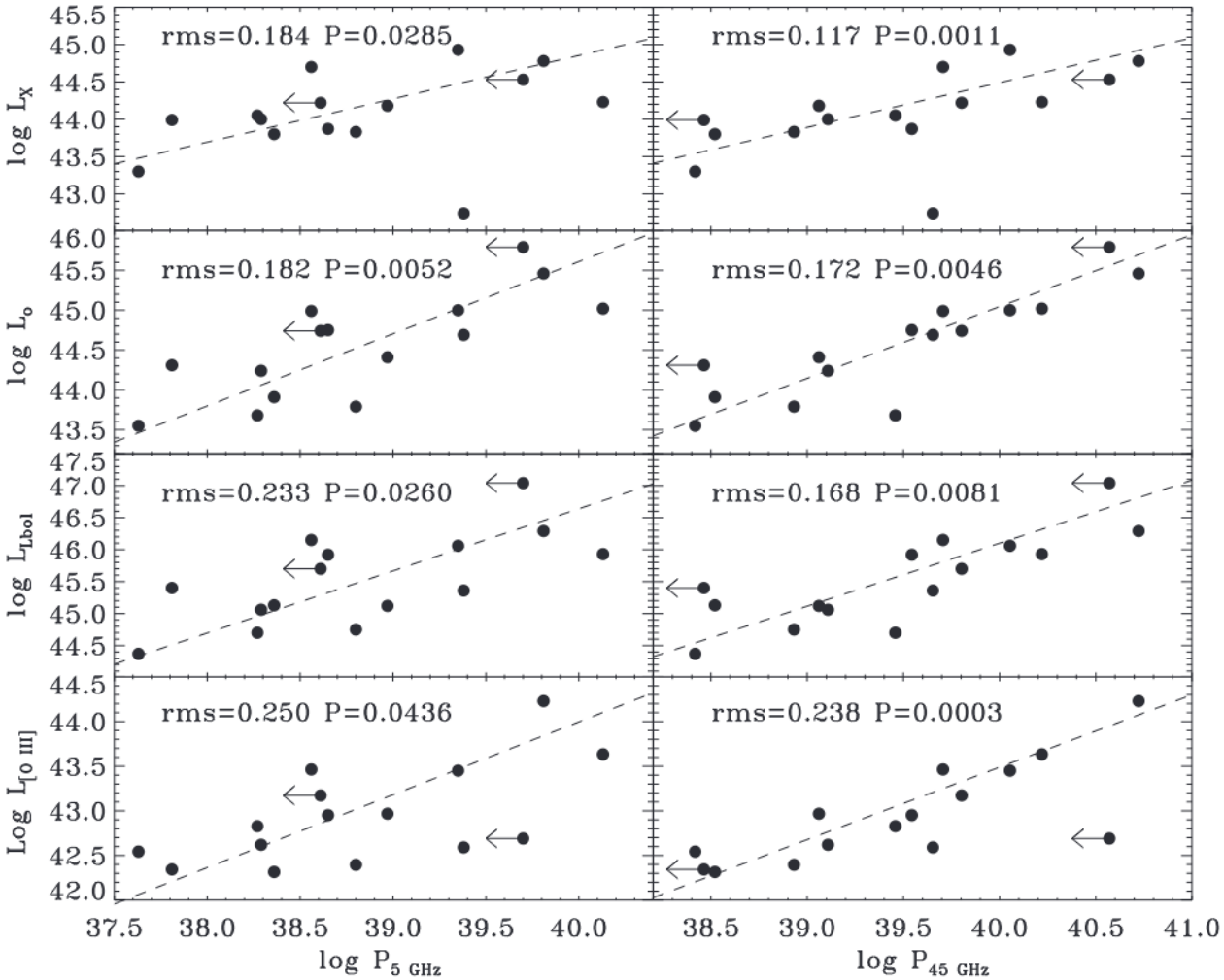

Figure 5. The relation between the radio core luminosities at 5 and 45 GHz (erg s^{-1}) and the X-ray (2–10 keV), optical, bolometric and [O III] line luminosities (erg s^{-1}) for the 15 PG RQQs. The value in the upper part of each panel expresses the rms scatter of the relation (assuming the upper limits as detections) and the generalized Kendall's τ test probability (P) of a fortuitous correlation. Note that the relations with $P_{45\ \mathrm{GHz}}$ are generally tighter, and the tightest relation is with L_X. The outlier PG 1001+054 with $L_X < 10^{43}$ erg s^{-1} is known to be significantly X-ray absorbed (Schartel et al. 2005), and was not considered in fitting the X-ray–radio relations.

a quasar regime (Sani et al. 2010). At 45 GHz, in this scenario the radio emission could primarily powered by free–free emission from discrete H II regions on sub-kpc scale, making it an excellent tracer of massive SF (Murphy et al. 2018). The expected SF rate estimated in this radio band is ~0.6–60 M$_\odot$ yr^{-1} (equation 15 from Murphy et al. 2011, assuming electron temperature of 10^4 K and a flat-spectrum non-thermal component), which is not far from what has been found in luminous quasar hosts (Jarvis et al. 2020; Shangguan et al. 2020) but is generally considered insufficient to explain the observed radio emission from quasars by an order of magnitude (Zakamska & Greene 2014; Zakamska et al. 2016). Nevertheless, the morphological compactness of the radio emission and the multiband correlations of the radio luminosities with AGN parameters (M_{BH}, L_{bol}, L/L_{Edd}) argue against SF as the origin of the high-frequency radio emission in PG RQQs.

(ii) *Disc wind*. An AGN-driven wind interacting with the ISM and the consequent shock acceleration can cause synchrotron emission (see models from Jiang et al. 2010; Nims et al. 2015). The optically thin radio emission is expected from an outflowing plasma from a standard accretion disc (Shakura & Sunyaev 1973) with high radiation pressure, generally related to a high L/L_{Edd}. Such scenario would explain the relation between steep spectral slopes and the high L/L_{Edd} and large bolometric luminosities. A faster wind being accelerated by higher continuum-scattering (i.e. higher Eddington ratio; Gofford et al. 2015) will produce stronger shocks which will accelerate more electrons, resulting in higher radio luminosities. The most luminous radio sources would approximately lie on the relation between the radio luminosity and the [O III] line width established by Zakamska & Greene (2014),[8] interpreted as synchrotron radio emission form quasar-driven winds propagating into the ISM of the host galaxy. A steep radio spectrum would be consistent with

[8]To be consistent with the line width – $L_{1.4\mathrm{GHz}}$ relation introduced by Zakamska & Greene (2014) for obscured quasars, we derive the velocity width containing 90 per cent of [O III] line, by assuming the conservative scenario where line is blueshifted and [O III] and Hβ widths are similar (Hβ are slightly [8 per cent] systematically narrower than [O III] on average; Zakamska & Greene 2014). In addition, we derive the 1.4-GHz luminosities from our measurements, assuming a flat-spectrum synchrotron component with a slope of 0.5. Therefore, this method with several assumptions provides an approximate estimate of the radio emission from a disc wind model for our sample.

Table 5. Statistical censored analysis of the tested correlations for RQQs and RLQs.

X (1)	Y (2)	Fig. (3)	sample (4)	Stat (5)	ρ_{XY} (6)	$P_{\rho_{XY}}$ (7)	rms (8)	Slope (9)	Intercept (10)
$\log P_{5\ \mathrm{GHz}}$	$\log L_{\mathrm{X}}$	5	RQQ	K	0.857	0.0285	0.184	0.58 ± 0.24	21.6 ± 8.1
$\log P_{45\ \mathrm{GHz}}$	$\log L_{\mathrm{X}}$	5	RQQ	K	1.209	0.0011	0.117	0.60 ± 0.20	20.5 ± 7.6
$\log P_{5\ \mathrm{GHz}}$	$\log L_{\mathrm{o}}$	5	RQQ	K	0.933	0.0052	0.182	0.91 ± 0.29	9.4 ± 8.9
$\log P_{45\ \mathrm{GHz}}$	$\log L_{\mathrm{o}}$	5	RQQ	K	1.009	0.0046	0.172	0.90 ± 0.29	9.0 ± 6.1
$\log P_{5\ \mathrm{GHz}}$	$\log L_{\mathrm{bol}}$	5	RQQ	K	0.743	0.0260	0.233	0.97 ± 0.32	7.8 ± 9.1
$\log P_{45\ \mathrm{GHz}}$	$\log L_{\mathrm{bol}}$	5	RQQ	K	0.933	0.0081	0.168	0.99 ± 0.34	6.7 ± 9.5
$\log P_{5\ \mathrm{GHz}}$	$\log L_{[\mathrm{O\ III}]}$	5	RQQ	K	0.705	0.0436	0.250	0.816 ± 0.25	11.4 ± 13.6
$\log P_{45\ \mathrm{GHz}}$	$\log L_{[\mathrm{O\ III}]}$	5	RQQ	K	1.276	0.0003	0.238	0.811 ± 0.19	11.0 ± 12.5
$\log M_{\mathrm{BH}}$	$\log P_{5\ \mathrm{GHz}}$	7	RQQ	K	0.5902	0.0746	0.469	1.17 ± 0.35	29.7 ± 19.1
$\log M_{\mathrm{BH}}$	$\log P_{45\ \mathrm{GHz}}$	7	RQQ	K	1.0095	0.0023	0.297	1.17 ± 0.28	30.3 ± 33.7
$\log M_{\mathrm{BH}}$	$\log P_{5\ \mathrm{GHz}}$	7	RLQ	P	0.576	0.066			
$\log M_{\mathrm{BH}}$	$\log P_{45\ \mathrm{GHz}}$	7	RLQ	K	0.2167	0.5352			
$\log H\beta\ FWHM$	$\alpha_{5-45\ \mathrm{GHz}}$	8	RQQ	K	0.8791	0.0258			
$\log H\beta\ FWHM$	$\alpha_{5-45\ \mathrm{GHz}}$	8	RLQ	K	-0.850	0.0215			
$\log L/L_{\mathrm{Edd}}$	$\alpha_{5-45\ \mathrm{GHz}}$	8	RQQ	K	-0.593	0.132			
$\log L/L_{\mathrm{Edd}}$	$\alpha_{5-45\ \mathrm{GHz}}$	8	RLQ	K	0.0167	0.964			
$\log M_{\mathrm{BH}}$	$\alpha_{5-45\ \mathrm{GHz}}$	8	RQQ	K	0.725	0.0655			
$\log M_{\mathrm{BH}}$	$\alpha_{5-45\ \mathrm{GHz}}$	8	RLQ	K	-0.567	0.125			
$\log L/L_{\mathrm{Edd}}$	$\log P_{45\ \mathrm{GHz}}/L_{\mathrm{o}}$	9	RQQ	K	-0.991	0.0093	0.245	-0.90 ± 0.36	-5.5 ± 4.1
$\log L/L_{\mathrm{Edd}}$	$\log P_{45\ \mathrm{GHz}}/L_{\mathrm{o}}$	9	RLQ	K	0.0381	0.903			
$\log M_{\mathrm{BH}}$	$\log P_{45\ \mathrm{GHz}}/L_{\mathrm{X}}$	9	RQQ	K	0.7619	0.0078	0.322	0.90 ± 0.37	-11.7 ± 7.2
$\log M_{\mathrm{BH}}$	$\log P_{45\ \mathrm{GHz}}/L_{\mathrm{X}}$	9	RLQ	K	-0.350	0.3387			

Note. Column description: (1)–(2) the two variables of the considered relation; (3) Figure; (4) sample (RQQ or RLQ) for the tested correlation. (5)–(6)–(7) the statistical analysis used for the given sub-sample to calculate the associated linear regression coefficient ρ_{XY} and the probability that there is no correlation $P_{\rho_{XY}}$: K for the censored generalized Kendall's τ correlation coefficient and P for the Pearson correlation coefficient for a fully detected data set; (8) the rms scatter of the linear regression; (9)–(10) the slope and the intercept of the best fits with their 1σ errors.

Table 6. Radio properties of the PG RLQ sample.

PG name	Alternative	F_{core}	$P_{45\ \mathrm{GHz}}$
PG 0007+106	MRK 1501	$2.6 \pm 1.0^{a,b,c}$ Jy	43.32
PG 1226+023	3C 273	26.9 ± 10.8^{a} Jy	44.89
PG 1302−102	PKS 1302−102	$0.59 \pm 0.07^{a,d}$ Jy	43.78
PG 1545+210	3C 323.1	$<2.6^{a}$ mJy	<42.27
PG 1704+608	3C 351	$<2.2^{a}$ mJy	<42.61
PG 2209+184	II Zw 171	37.6 ± 17.2^{a} mJy	41.25
PG 1103−006	PKS 1106−0052	67.65 ± 14.4^{e} mJy	43.27
PG 1512+370	4C +37.43	15.0^{f} mJy	42.47
PG 0003+158	PKS 0003+15	56 mJy	43.25
PG 1004+130	4C +13.41	79 mJy	42.76
PG 1048−090	3C 246	148 mJy	43.40
PG 1100+772	3C 249.1	110 mJy	43.16
PG 1309+355		25 mJy	42.00
PG 1425+267	B2 1425+26	25 mJy	42.68
PG 2251+113	4C +11.72	79 mJy	43.06
PG 2308+098	4C +09.72	34 mJy	42.99

Note. Column description: (1)–(2) PG source name and alternative name; (3)–(4) radio core flux densites and luminosities (erg s^{-1}) obtained from Q-band radio maps (upper list) and extrapolated by fitting the radio SED taken from NED (lower list) (See Section 3.2 for details); references: [a]NVAS (NRAO VLA Archive Survey), [b]Gu, Cao & Jiang (2009), [c]Lanyi et al. (2010), [d]Perley & Meisenheimer (2017), [e]Sajina et al. (2011), [f]Bolton et al. (2004); (4) 45-GHz core luminosity (erg s^{-1}). The typical error of the core flux densities of RLQs derived from their radio SED is approximately a factor ∼2 of the measurements.

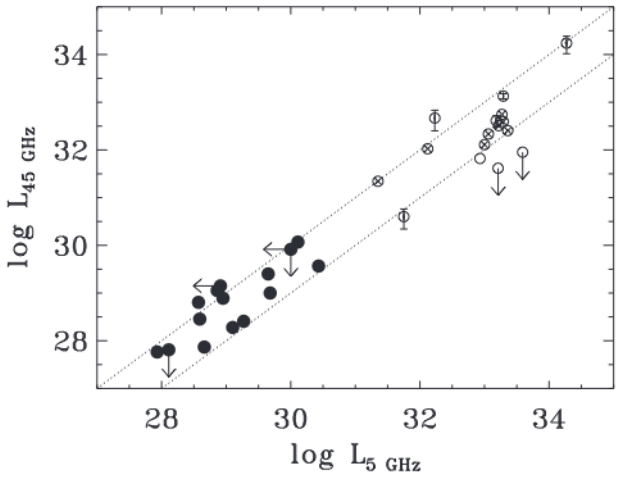

Figure 6. The 5-GHz radio core luminosities versus the 45-GHz luminosity (erg s^{-1} Hz^{-1}). The filled points are the 15 RQQs, the empty points are the RLQs with available VLA Q-band data and the crossed empty circles are the RLQs with the 45-GHz flux densities extrapolated from their radio spectra. The RLQs are typically ∼1000 more luminous than the RQQs at both 5 GHz and 45 GHz. The dotted lines are drawn to visualize a scatter of a factor of 10. The scatter of RQQs ($\sigma = 0.29$) is smaller than that of RLQs ($\sigma = 0.41$).

synchrotron emission from a diffuse disc wind on the scale of the galaxy. Moreover, the radio production based on this mechanism is not predicted to depend directly on M_{BH}, in contrast with our results. In conclusion, we cannot fully rule out the possibility that the

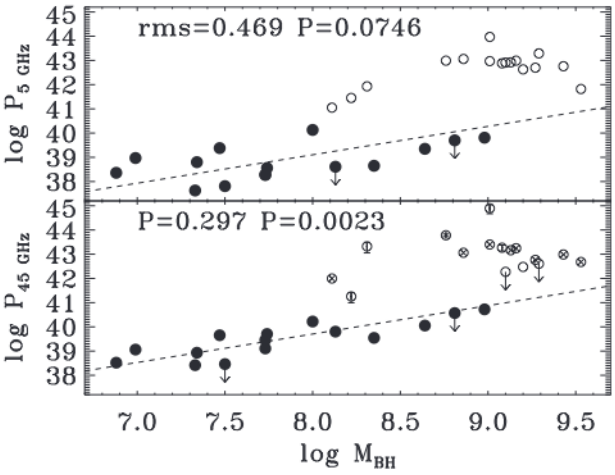

Figure 7. $M_{\rm BH}$ (in $M_\odot$) versus $P_{5\,\rm GHz}$ (upper panel) and versus $P_{45\,\rm GHz}$ (lower panel) in units of erg s^{-1}. The filled points are the 15 RQQs, the empty points are the RLQs with available VLA Q band data and the crossed empty circles are the RLQ with the 45-GHz flux densities extrapolated from their radio spectra. The value of the generalized Kendall's τ test probability (P) for the RQQ relation and its rms is provided in each panel. Note the tight relation of $P_{45\,\rm GHz}$ and $M_{\rm BH}$ valid for RQQs.

45-GHz radio luminosities of the high-Eddington luminous PG RQQs have a significant contribution from a disc wind.

(iii) *Jet*. An uncollimated sub-relativistic jet, whose power is scaled down with respect to the jets in RLQs, is another possible scenario. As already discussed by Laor et al. (2019), an orientation dependence of the radio properties similar to that interpreted for the RLQ unification scheme would lead to an opposite relation between the observed spectral slope and the Hβ width: in the case of a type-1 AGN by definition, low inclination would tend to show smaller line widths and flatter radio spectra (an isotropically emitting outflow could still be possible). The observed $M_{\rm BH}$ correlation with the radio luminosity and radio-loudness is consistent with the idea of a jet lunching mechanism by extracting energy from a spinning supermassive BH, specifically the Blandford–Znajek process (Blandford & Znajek 1977). A large BH masses and low Eddington ratios a core-brightened jet component is possibly emerging in the radio band, in agreement with what has been found for local Seyferts Baldi et al. (2021b). However, we do not find any continuity of the radio properties between the RQQs and the RLQs of the sample,[9] excluding any possible result bias due to the incompleteness of the sample or because they come from the same original PG sample. Furthermore, the RLQs reveal a hint of reverse trends to the radio-based correlations shown by RQQs, suggesting different driving mechanisms of radio production.

(iv) *Coronal wind*. A magnetically active corona linked to an accretion disc can produce synchrotron radio emission from the accelerated relativistic electrons produced by magnetic reconnection (Laor & Behar 2008; Raginski & Laor 2016). A dependence of the radio production on the X-ray power, produced by the cooling electrons, and the Eddington ratio is expected. In fact, the high-frequency radio emission tightly correlates with high-energy nuclear component, suggesting a causal common emitting region, i.e. corona.

[9]It is still not clear whether a bimodal or continuous radio-loudness distribution of RQ and RL AGN would be distinct in the radio properties of the two classes (in terms of e.g. kinetic luminosity, size, speeds) (e.g. Kellermann et al. 1989; Cirasuolo et al. 2003; Ho 2008; Macfarlane et al. 2021).

The observed radio to X-ray luminosity ratio agrees with the 10^{-5} ratio found for the analogous active coronae in cool active stars (Güdel & Benz 1993). Highly active coronae, associated with high $L/L_{\rm Edd}$, are able to produce extended radio emission with an optically thin bubble emerging from the outflowing corona similar to a Coronal Mass Ejection. At higher X-ray luminosities, the height of the corona would increase (Alston et al. 2020) with a higher probability of outflowing. At low $L/L_{\rm Edd}$, the radio emission is only related to the flat-spectrum self-absorbed emission emanated by an unresolved corona. When the Compton scattering is the dominant cooling mechanism, the luminosities from the corona should follow $\propto M_{\rm BH}$ (Taam et al. 2008; Liu & Liu 2009), consistent with the present results at 45 GHz.

Based on our result, the most probable scenarios to account for the radio properties of PG RQQs is that their radio cores originate from non-thermal relativistic electrons likely accelerated in an active corona, where intense magnetic reconnection events occur. However, a possible increment of the emission contribution from a weak jet, as the BH mass increases, cannot be ruled out, similarly to the jet power dependence on $M_{\rm BH}$ observed in RL AGN (Liu, Jiang & Gu 2006), although the role of such a quantity in characterizing the RQ AGN properties is still controversial (e.g. Boroson 2002; Metcalf & Magliocchetti 2006; Gürkan et al. 2019; Baldi et al. 2021b; Macfarlane et al. 2021). In our case, this interpretation will accommodate the flat-spectrum cores we observe at low $L/L_{\rm Edd}$ and large BH masses. In addition, the most luminous quasars at high Eddington ratios could have an important contribution in the radio band from disc winds. In fact, when the AGN disc is able to drive strong winds due to high radiation pressure, optically thin intense steep-spectrum radio emission can be emanated either by the accretion disc itself or from the outflowing corona. The absence of such outflowing component at low $L/L_{\rm Edd}$ is due to the decreasing of the radiation pressure and thus its relative radio contribution, which make the flat-spectrum core emerges over the steep-spectrum component. Nevertheless, it appears clear that a nuclear star-forming core does not appear to reconcile with our results and with a general interpretation of the radio emission in type-1 QSOs (Zakamska et al. 2016).

4.2 Comparison with X-ray binary systems

Since jets are observed across all types of active BHs, it is interesting to ask whether there are any similarities between the radio properties of the RQQs and those of XRBs and hence whether RQQs correspond to any particular X-ray 'state' of XRBs. Fender, Belloni & Gallo (2004) provide a full description of the change of radio luminosity with 'state'. In the low/hard X-ray state where, very broadly, the accretion rate is low or only moderate and the accretion is probably radiatively inefficient, there is steady and relatively powerful radio emission from a jet, with radio and X-ray luminosities being well correlated (e.g. Corbel et al. 2013). Although not the only possible interpretation, the correlations shown in Fig. 5 are quite consistent with such a scenario. At very high accretion rates, i.e. the soft X-ray state where the accretion is radiatively efficient, there is no detectable radio emission. For example, the persistent soft-state XRB 4U1957 + 11 (Maccarone et al. 2020) is undetected in radio maps with noise level of 1.07 μJy beam^{-1}, while at a 2–20 keV X-ray flux of 10^{-9} erg cm^{-2} s^{-1}. The radio/X-ray ratio for the present PG RQQs is 10^{-5} far greater than value for XRBs.

Part of the increased radio emission in RQQs with respect to XRBs may be due to the BH mass dependence in core-dominated

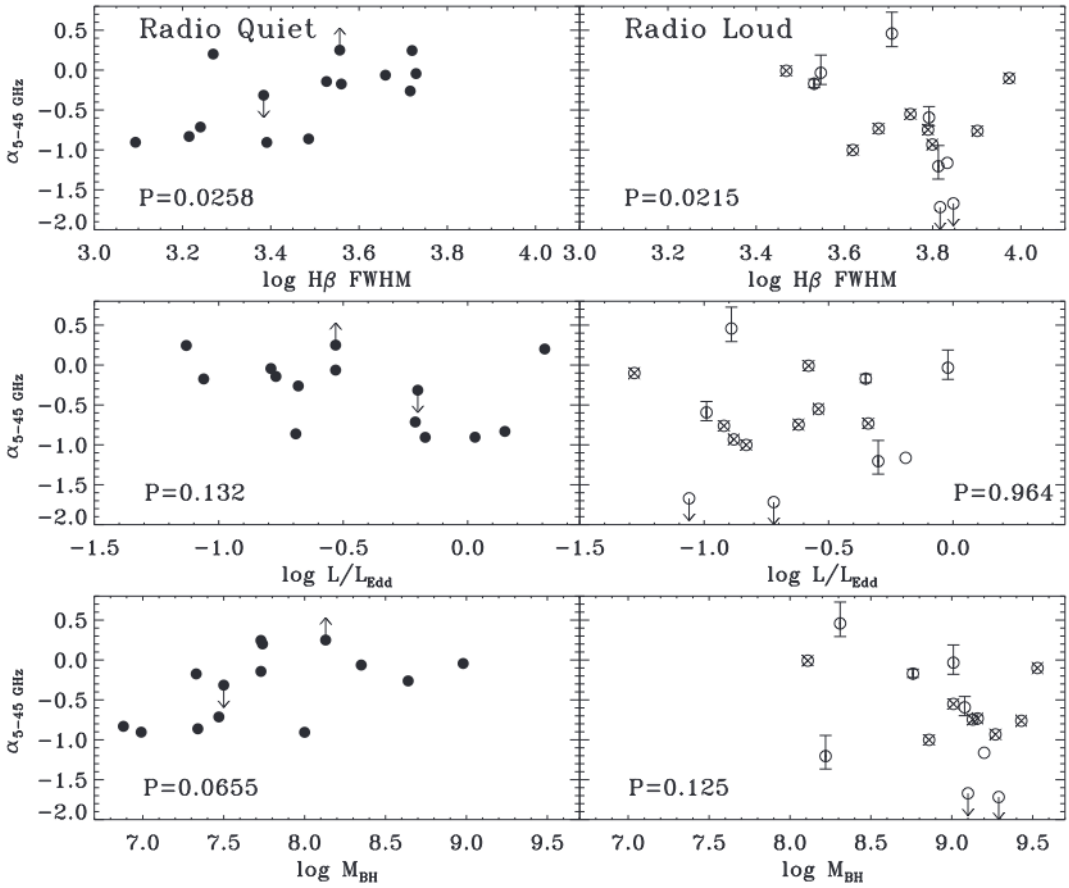

Figure 8. The radio spectral index derived between 5 and 45 GHz as function of the Hβ FWHM (km s^{-1}), L/L_{Edd} and M_{BH} ($M_\odot$). The left-hand panels show the 15 PG RQQs, whereas the right-hand panels show the 16 PG RLQs. The filled points are the PG RQQs, while the empty points are the PG RLQs. Those with crosses are the PG RLQs whose 45-GHz radio luminosities have been estimated by fitting their radio SED. The value in the lower left corner of each panel expresses the generalized Kendall's τ test probability (P) of a fortuitous correlation and its rms. The strongest trends are with the Hβ FWHM, but are opposite in RQQs and RQQs, suggesting different emission mechanisms.

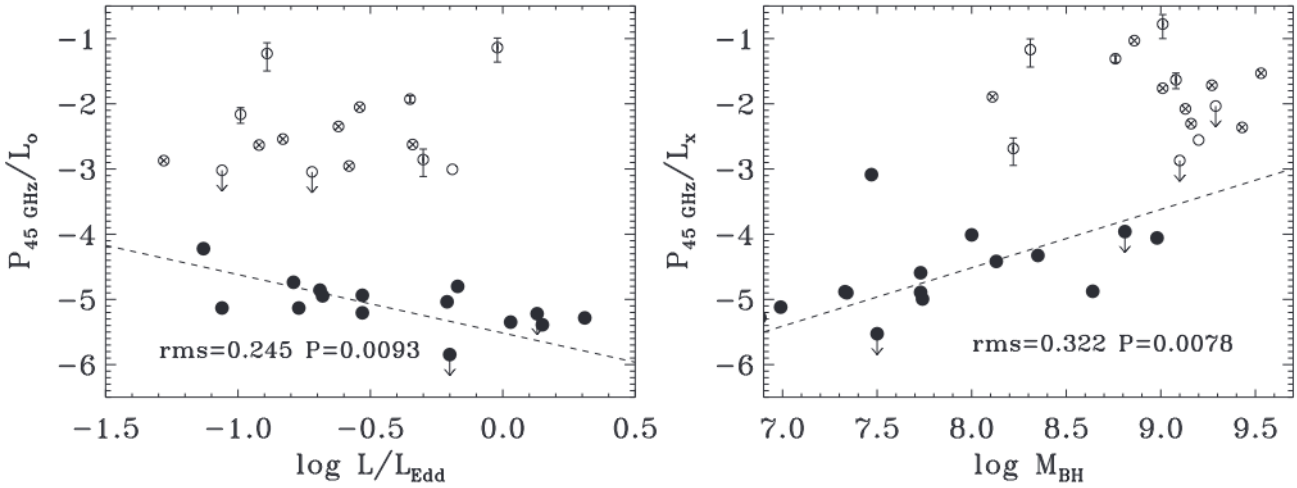

Figure 9. Left-hand panel: radio loudness estimated as ratio between 45-GHz and optical luminosities versus L/L_{Edd}. Right-hand panel: radio loudness estimated as ratio between 45-GHz and 2–10 keV X-ray luminosities versus M_{BH} ($M_\odot$). The filled points are the PG RQQs, while the empty points are the PG RLQs. Those with crosses are the PG RLQs whose 45-GHz radio luminosities have been estimated by fitting their radio SED. The value in the lower part of each panel expresses the rms and the generalized Kendall's τ test probability (P) of a fortuitous correlation for the RQQs. Note that the 45 GHz-based radio-loudness decreases with increasing L/L_{Edd}, while the X-ray based radio-loudness increases towards higher M_{BH}, with a jump by a factor of ~30 at $M_{BH} > 10^9$ $M_\odot$, where all the PG quasars become RL.

jets. Heinz & Sunyaev (2003) argue that AGN should be 3–4 orders of magnitude more radio loud than XRBs. However, with radio flux densities 3 or 4 orders of magnitude above the upper limit for 4U1957+11, and X-ray fluxes about 2 orders of magnitude less than that of 4U1957+11, the PG RQQs are still at least 1–2 orders of magnitude more radio loud than expected if they were soft-state XRBs, even taking account of the mass dependence. Consequently, RQQs are probably not simply soft-state systems (see Davis & Tchekhovskoy 2020).

The increase of radio luminosity with BH mass seen in our sample is consistent with at least a contribution from a compact jet in the radio emission in a hard-state scenario. Conversely, a decrease in radio luminosity with increasing accretion rate is not consistent with a jet scenario (Heinz & Sunyaev 2003), at least if the RQQs remain in the hard state. However, the variation of radio luminosity with accretion rate and BH mass in RQQs, differently from XRB states, likely indicates a complexity of different accretion-ejection modes (e.g. Baldi et al. 2021b; Fernández-Ontiveros & Muñoz-Darias 2021) and that at least two sources of radio emission co-exist for RQQs.

5 CONCLUSIONS

This initial study (15 targets) of a comprehensive radio survey of the PG RQQs (71 objects), named PG-RQS, reveals the following main results.

(i) The 45-GHz emission is detected in 13 out of 15 PG RQQs, is generally unresolved, implying a source smaller than typically 50–100 pc.

(ii) The high-frequency emission in PG RQQs is generally characterized by a flat-spectrum component, which indicates a compact optically thick source.

(iii) The 45-GHz luminosity is tightly correlated with the AGN nuclear strength (X-ray, optical, [O III], bolometric luminosities), suggesting an origin at the accretion disc scale. The 45-GHz luminosity is also correlated with BH mass.

(iv) The radio spectral properties of RQQs marginally correlate with AGN parameters: a flat-spectrum core emerges at low Eddington ratios, large BH masses, and small Hβ widths.

(v) The 45 GHz-based radio loudness decreases with increasing Eddington ratio and decreasing BH mass.

The most plausible scenario to account for the general properties of the compact 45-GHz cores detected in our sample is synchrotron emission from a magnetically active X-ray coronae. However, at high Eddington ratios and large BH masses a radio-emission contribution from a disc wind and weak jet, respectively, cannot be ruled out. These preliminary intriguing results need to be verified by extending this study to the complete sample of the 71 PG RQQs, which will help us to improve the statistical significance of the weak regressions found in this work. Further studies, within the PG-RQS survey, at higher resolution using the VLBI technique, together with an expanded spectral coverage from low frequencies using *GMRT* and *LOFAR* observatories, to the mm and sub-mm regime using *ALMA*, will likely allow to determine the range of radio emission mechanism in RQ AGN, and shed new light on a host of physical processes from SF on kpc scale down to the coronal structure on milli-pc scale. The future step will be the advent of *SKA*, which will survey vast numbers of local RQ active galaxies with μJy-sensitivity at low and intermediate radio frequencies (Orienti et al. 2015), providing the cornerstone of our understanding of radio emission across a wide range of galaxy types and accretion properties.

ACKNOWLEDGEMENTS

We thank the anonymous referee for his/her helpful comments to improve the manuscript. AH acknowledges support by the I-Core Program of the Planning and Budgeting Committee and the Israel Science Foundation, and support by ISF grant 647/18. This research was supported by grant no. 2018154 from the United States-Israel Binational Science Foundation (BSF). AL acknowledges support by the Israel Science Foundation (grant no. 1008/18). EB was funded by a Center of Excellence of The Israel Science Foundation (grant no. 2752/19). IM acknowledges support from STFC under ST/R000638/1. The National Radio Astronomy Observatory is a facility of the National Science Foundation operated under cooperative agreement by Associated Universities, Inc.

DATA AVAILABILITY

The radio data used in this work have been obtained by the VLA. The uncalibrated data set is public and available from the VLA data archive (project 16B-126). Calibrated image products are available upon reasonable request to the corresponding author.

REFERENCES

Alston W. N. et al., 2020, Nat. Astron., 4, 597
Baldi R. D., Behar E., Laor A., Horesh A., 2015, MNRAS, 454, 4277
Baldi R. D. et al., 2018, MNRAS, 476, 3478
Baldi R. D. et al., 2021a, MNRAS, 500, 4749
Baldi R. D. et al., 2021b, MNRAS, 508, 2019
Barvainis R., Antonucci R., 1989, ApJS, 70, 257
Barvainis R., Lonsdale C., Antonucci R., 1996, AJ, 111, 1431
Barvainis R., Lehár J., Birkinshaw M., Falcke H., Blundell K. M., 2005, ApJ, 618, 108
Baskin A., Laor A., 2005, MNRAS, 356, 1029
Baskin A., Laor A., 2021, MNRAS, 508, 680
Becker R. H., White R. L., Helfand D. J., 1995, ApJ, 450, 559
Behar E., Baldi R. D., Laor A., Horesh A., Stevens J., Tzioumis T., 2015, MNRAS, 451, 5036
Behar E., Vogel S., Baldi R. D., Smith K. L., Mushotzky R. F., 2018, MNRAS, 478, 399
Behar E. et al., 2020, MNRAS, 491, 3523
Berriman G., Schmidt G. D., West S. C., Stockman H. S., 1990, ApJS, 74, 869
Best P. N., Kauffmann G., Heckman T. M., Brinchmann J., Charlot S., Ivezić Ž., White S. D. M., 2005, MNRAS, 362, 25
Bian W.-H., Chen Y.-M., Hu C., Huang K., Xu Y., 2008, Chinese J. Astron. Astrophys., 8, 522
Blandford R. D., Znajek R. L., 1977, MNRAS, 179, 433
Blandford R., Meier D., Readhead A., 2019, ARA&A, 57, 467
Blundell K. M., Beasley A. J., 1998, MNRAS, 299, 165
Blundell K. M., Beasley A. J., Lacy M., Garrington S. T., 1996, ApJ, 468, L91
Bolton R. C. et al., 2004, MNRAS, 354, 485
Boroson T. A., 2002, ApJ, 565, 78
Boroson T. A., Green R. F., 1992, ApJS, 80, 109
Brandt W. N., Laor A., Wills B. J., 2000, ApJ, 528, 637
Cattaneo A., Best P. N., 2009, MNRAS, 395, 518
Chang N., Xie F. G., Liu X., Ho L. C., Dong A. J., Han Z. H., Wang X., 2021, MNRAS, 503, 1987
Chiaraluce E., Bruni G., Panessa F., Giroletti M., Orienti M., Rampadarath H., Vagnetti F., Tombesi F., 2019, MNRAS, 485, 3185
Chiaraluce E., Panessa F., Bruni G., Baldi R. D., Behar E., Vagnetti F., Tombesi F., McHardy I., 2020, MNRAS, 495, 3943
Cirasuolo M., Celotti A., Magliocchetti M., Danese L., 2003, MNRAS, 346, 447

Condon J. J., Cotton W. D., Greisen E. W., Yin Q. F., Perley R. A., Taylor G. B., Broderick J. J., 1998, AJ, 115, 1693
Condon J. J., Kellermann K. I., Kimball A. E., Ivezić Ž., Perley R. A., 2013, ApJ, 768, 37
Corbel S., Coriat M., Brocksopp C., Tzioumis A. K., Fender R. P., Tomsick J. A., Buxton M. M., Bailyn C. D., 2013, MNRAS, 428, 2500
Davis S. W., Laor A., 2011, ApJ, 728, 98
Davis S. W., Tchekhovskoy A., 2020, ARA&A, 58, 407
Doi A., Kameno S., Kohno K., Nakanishi K., Inoue M., 2005, MNRAS, 363, 692
Doi A., Nakanishi K., Nagai H., Kohno K., Kameno S., 2011, AJ, 142, 167
Doi A., Asada K., Fujisawa K., Nagai H., Hagiwara Y., Wajima K., Inoue M., 2013, ApJ, 765, 69
Falcke H., Lehár J., Barvainis R., Nagar N. M., Wilson A. S., 2001, in Peterson B. M., Pogge R. W., Polidan R. S., eds, ASP Conf. Ser. Vol. 224, Probing the Physics of Active Galactic Nuclei. Astron. Soc. Pac., San Francisco, p. 265
Fawcett V. A., Alexander D. M., Rosario D. J., Klindt L., Fotopoulou S., Lusso E., Morabito L. K., Calistro Rivera G., 2020, MNRAS, 494, 4802
Fender R. P., Belloni T. M., Gallo E., 2004, MNRAS, 355, 1105
Fernández-Ontiveros J. A., Muñoz-Darias T., 2021, MNRAS, 504, 5726
Field G. B., Rogers R. D., 1993, ApJ, 403, 94
Gallimore J. F., Baum S. A., O'Dea C. P., 1997, Nature, 388, 852
Gallimore J. F., Axon D. J., O'Dea C. P., Baum S. A., Pedlar A., 2006, AJ, 132, 546
Giroletti M., Panessa F., 2009, ApJ, 706, L260
Gofford J., Reeves J. N., McLaughlin D. E., Braito V., Turner T. J., Tombesi F., Cappi M., 2015, MNRAS, 451, 4169
Gu M., Cao X., Jiang D. R., 2009, MNRAS, 396, 984
Guainazzi M., Jimenez-Bailon E., Piconcelli E., 2006, in Gaskell C. M., McHardy I. M., Peterson B. M., Sergeev S. G., eds, AGN Variability from X-Rays to Radio Waves ASP Conf. Ser., Vol. 360. Astronomical Society of the Pacific, San Francisco, p. 123
Güdel M., Benz A. O., 1993, ApJ, 405, L63
Güdel M., Audard M., Smith K. W., Behar E., Beasley A. J., Mewe R., 2002, ApJ, 577, 371
Gürkan G. et al., 2019, A&A, 622, A11
Haas M. et al., 2003, A&A, 402, 87
Heckman T. M., Best P. N., 2014, ARA&A, 52, 589
Heinz S., Sunyaev R. A., 2003, MNRAS, 343, L59
Ho L. C., 2002, ApJ, 564, 120
Ho L. C., 2008, ARA&A, 46, 475
Inoue Y., Doi A., 2014, PASJ, 66, L8
Inoue Y., Doi A., 2018, ApJ, 869, 114
Isobe T., Feigelson E. D., Akritas M. G., Babu G. J., 1990, ApJ, 364, 104
Jarvis M. E. et al., 2019, MNRAS, 485, 2710
Jarvis M. E. et al., 2020, MNRAS, 498, 1560
Jarvis M. E. et al., 2021, MNRAS, 503, 1780
Jiang Y.-F., Ciotti L., Ostriker J. P., Spitkovsky A., 2010, ApJ, 711, 125
Kaspi S., Smith P. S., Netzer H., Maoz D., Jannuzi B. T., Giveon U., 2000, ApJ, 533, 631
Kellermann K. I., Sramek R., Schmidt M., Shaffer D. B., Green R., 1989, AJ, 98, 1195
Kellermann K. I., Sramek R. A., Schmidt M., Green R. F., Shaffer D. B., 1994, AJ, 108, 1163
Kendall M., 1983, Biometrika, 30, 81
King A. L. et al., 2013, ApJ, 762, 103
Kukula M. J., Pedlar A., Baum S. A., O'Dea C. P., 1995, MNRAS, 276, 1262
Kukula M. J., Dunlop J. S., Hughes D. H., Rawlings S., 1998, MNRAS, 297, 366
Lacy M., Laurent-Muehleisen S. A., Ridgway S. E., Becker R. H., White R. L., 2001, ApJ, 551, L17
Lanyi G. E. et al., 2010, AJ, 139, 1695
Lanzuisi G. et al., 2014, ApJ, 781, 105
Laor A., 1998, ApJ, 505, L83
Laor A., 2000, ApJ, 543, L111
Laor A., Behar E., 2008, MNRAS, 390, 847
Laor A., Baldi R. D., Behar E., 2019, MNRAS, 482, 5513
Lavalley M., Isobe T., Feigelson E., 1992, in Worrall D. M., Biemesderfer C., Barnes J., eds, ASP Conf. Ser. Vol. 25, Astronomical Data Analysis Software and Systems I. Astron. Soc. Pac., San Francisco, p. 245
Leipski C., Falcke H., Bennert N., Hüttemeister S., 2006, A&A, 455, 161
Liu Y., Jiang D. R., Gu M. F., 2006, ApJ, 637, 669
Liu J.-Y., Liu B.-F., 2009, Res. Astron. Astrophys., 9, 966
Maccarone T. J., Osler A., Miller-Jones J. C. A., Atri P., Russell D. M., Meier D. L., McHardy I. M., Longa-Peña P. A., 2020, MNRAS, 498, L40
Macfarlane C. et al., 2021, MNRAS, 506, 5888
McLure R. J., Jarvis M. J., 2004, MNRAS, 353, L45
Maini A., Prandoni I., Norris R. P., Giovannini G., Spitler L. R., 2016, A&A, 589, L3
Mancuso C. et al., 2017, ApJ, 842, 95
Markoff S., Nowak M. A., Wilms J., 2005, ApJ, 635, 1203
Markowitz A., Edelson R., 2004, ApJ, 617, 939
Merloni A., Heinz S., di Matteo T., 2003, MNRAS, 345, 1057
Metcalf R. B., Magliocchetti M., 2006, MNRAS, 365, 101
Middelberg E. et al., 2004, A&A, 417, 925
Miller P., Rawlings S., Saunders R., 1993, MNRAS, 263, 425
Mundell C. G., Ferruit P., Nagar N., Wilson A. S., 2009, ApJ, 703, 802
Murphy T. et al., 2010, MNRAS, 402, 2403
Murphy E. J. et al., 2011, ApJ, 737, 67
Murphy E. J., Dong D., Momjian E., Linden S., Kennicutt R. C. J., Meier D. S., Schinnerer E., Turner J. L., 2018, ApJS, 234, 24
Nagar N. M., Wilson A. S., Mulchaey J. S., Gallimore J. F., 1999, ApJS, 120, 209
Nagar N. M., Falcke H., Wilson A. S., Ulvestad J. S., 2002, A&A, 392, 53
Nagar N. M., Falcke H., Wilson A. S., 2005, A&A, 435, 521
Nelson C. H., 2000, ApJ, 544, L91
Neugebauer G., Green R. F., Matthews K., Schmidt M., Soifer B. T., Bennett J., 1987, ApJS, 63, 615
Nims J., Quataert E., Faucher-Giguère C.-A., 2015, MNRAS, 447, 3612
Nyland K. et al., 2020, ApJ, 905, 74
Orienti M., D'Ammando F., Giroletti M., Giovannini G., Panessa F., 2015, in Proc. Advancing Astrophysics with the Square Kilometre Array (AASKA14). p. 87, Available at: http://pos.sissa.it/cgi-bin/reader/conf.cgi?confid=215
Padovani P., Miller N., Kellermann K. I., Mainieri V., Rosati P., Tozzi P., 2011, ApJ, 740, 20
Panessa F., Giroletti M., 2013, MNRAS, 432, 1138
Panessa F. et al., 2015, MNRAS, 447, 1289
Panessa F., Baldi R. D., Laor A., Padovani P., Behar E., McHardy I., 2019, Nat. Astron., 3, 387
Paolillo M., Schreier E. J., Giacconi R., Koekemoer A. M., Grogin N. A., 2004, ApJ, 611, 93
Park S., Sohn B. W., Yi S. K., 2013, A&A, 560, A80
Perley R. A., Meisenheimer K., 2017, A&A, 601, A35
Petric A. O., Ho L. C., Flagey N. J. M., Scoville N. Z., 2015, ApJS, 219, 22
Raginski I., Laor A., 2016, MNRAS, 459, 2082
Ricci R., Prandoni I., De Ruiter H. R., Parma P., 2019, A&A, 621, A19
Richards G. T., McCaffrey T. V., Kimball A., Rankine A. L., Matthews J. H., Hewett P. C., Rivera A. B., 2021, AJ, 162, 270
Saez C., Brandt W. N., Gallagher S. C., Bauer F. E., Garmire G. P., 2012, ApJ, 759, 42
Sajina A., Partridge B., Evans T., Stefl S., Vechik N., Myers S., Dicker S., Korngut P., 2011, ApJ, 732, 45
Sanders D. B., Phinney E. S., Neugebauer G., Soifer B. T., Matthews K., 1989, ApJ, 347, 29
Sani E., Lutz D., Risaliti G., Netzer H., Gallo L. C., Trakhtenbrot B., Sturm E., Boller T., 2010, MNRAS, 403, 1246
Schartel N., Rodríguez-Pascual P. M., Santos-Lleó M., Clavel J., Guainazzi M., Jiménez-Bailón E., Piconcelli E., 2005, A&A, 433, 455
Schmidt M., Green R. F., 1983, ApJ, 269, 352
Schmitt J. H. M. M., 1985, ApJ, 293, 178

Science Software Branch at STScI, 2012, Astrophysics Source Code Library, record ascl:1207.011
Shakura N. I., Sunyaev R. A., 1973, A&A, 24, 337
Shangguan J., Ho L. C., Bauer F. E., Wang R., Treister E., 2020, ApJ, 899, 112
Shi Y., Rieke G. H., Ogle P. M., Su K. Y. L., Balog Z., 2014, ApJS, 214, 23
Sikora M., Stawarz Ł., Lasota J.-P., 2007, ApJ, 658, 815
Smith K. L., Mushotzky R. F., Vogel S., Shimizu T. T., Miller N., 2016, ApJ, 832, 163
Smith K. L. et al., 2020a, MNRAS, 492, 4216
Smith K. L., Koss M., Mushotzky R., Wong O. I., Shimizu T. T., Ricci C., Ricci F., 2020b, ApJ, 904, 83
Taam R. E., Liu B. F., Meyer F., Meyer-Hofmeister E., 2008, ApJ, 688, 527
Talbot R. Y., Sijacki D., Bourne M. A., 2021, preprint (arXiv:2111.01801)
Tremaine S. et al., 2002, ApJ, 574, 740
Ulvestad J. S., Wong D. S., Taylor G. B., Gallimore J. F., Mundell C. G., 2005a, AJ, 130, 936
Ulvestad J. S., Antonucci R. R. J., Barvainis R., 2005b, ApJ, 621, 123
Vestergaard M., Peterson B. M., 2006, ApJ, 641, 689
Zakamska N. L., Greene J. E., 2014, MNRAS, 442, 784
Zakamska N. L. et al., 2016, MNRAS, 455, 4191

This paper has been typeset from a TEX/LATEX file prepared by the author.